

Generalization vs. Memorization in Autoregressive Deep Learning: Or, Examining Temporal Decay of Gradient Coherence

James Amarel¹, Nicolas Hengartner, Robyn Miller, Kamaljeet Singh, Siddharth Mansingh, Arvind Mohan, Benjamin Migliori, Emily Casleton, Alexei Skurikhin, Earl Lawrence, Gerd J. Kunde

Los Alamos National Laboratory, Los Alamos, NM 87545

¹jlamarel@lanl.gov

Abstract

Foundation models trained as autoregressive PDE surrogates hold significant promise for accelerating scientific discovery through their capacity to both extrapolate beyond training regimes and efficiently adapt to downstream tasks despite a paucity of examples for fine-tuning. However, reliably achieving genuine generalization - a necessary capability for producing novel scientific insights and robustly performing during deployment - remains a critical challenge. Establishing whether or not these requirements are met demands evaluation metrics capable of clearly distinguishing genuine model generalization from mere memorization.

We apply the influence function formalism to systematically characterize how autoregressive PDE surrogates assimilate and propagate information derived from diverse physical scenarios, revealing fundamental limitations of standard models and training routines in addition to providing actionable insights regarding the design of improved surrogates.

1 Introduction

Machine learning surrogate models have emerged as a powerful approach for efficiently approximating the solutions of computationally intensive partial differential equations (PDEs). These surrogate methods range from purely data-driven approaches, trained on high-fidelity simulation data, to physics-informed neural networks, which integrate PDE structures directly into the training loss, enforcing physical laws as soft constraints (Raissi, Perdikaris, and Karniadakis 2019). Such models hold promise for achieving significant computational acceleration in applications such as fluid dynamics (Takamoto et al. 2024; Lippe et al. 2023; Gupta and Brandstetter 2022; Ohana et al. 2025; Herde et al. 2024), climate modeling (Bodnar et al. 2024), and materials science (Batatia et al. 2024), enabling rapid research and development across diverse scientific and engineering disciplines. Despite these advances, reliable generalization and robustness remains a critical challenge (Krishnapriyan et al. 2021). Before surrogate models can be safely deployed in operational environments demanding generalization beyond their training data, it is essential to develop methods capable of quantifying risk profiles and ensuring predictions remain trustworthy.

Understanding the balance between memorization of training examples and genuine generalization is critical to

model robustness; diagnostic tools such as influence functions (Koh and Liang 2020; Bae et al. 2022), leverage scores, and gradient alignment analyses offer promising avenues for characterizing this balance, revealing whether models rely appropriately on generalized understanding or disproportionately on memorized patterns (Fort et al. 2020; Chatterjee 2020; Chatterjee and Zielinski 2022; Zielinski, Krishnan, and Chatterjee 2020).

Autoregressive models, useful for their promising extrapolation capabilities, accumulate errors during inference due to the inevitable distribution shift that originates with the using of model outputs as inputs to drive the predicted evolution arbitrarily far into the future (Lee 2023; Brandstetter, Worrall, and Welling 2023). The length of time that a model performs (and is confident) prior to excessive prediction error defines a “trust horizon” for forward prediction that is contingent on its encoding of the true data-generating mechanisms - the physics - rather than merely exploiting empirical correlations among proximal points in feature space to perform local statistical interpolation. Traditional benchmarks, such as point-wise mean squared error evaluations on limited validation datasets, often fail to adequately capture surrogate model reliability, especially when faced with inevitable distribution shifts arising from changes in initial or boundary conditions, mesh resolutions, or varying physical parameter regimes. Physics-informed metrics, including conservation-law violation assessments, PDE residual norms, analytical-limit checks, and numerical stability evaluations, have been proposed to better reflect model robustness (Karniadakis, Billionis, and Perdikaris 2021), yet even these enriched criteria may not fully quantify the true worst-case prediction errors. Indeed, empirical accuracy metrics based on finitely many examples can dramatically underestimate the true worst-case error, especially when the data is noisy, sparse, or incompletely understood.

In scientific machine learning, limited availability of high-fidelity simulation data often results in narrow training distributions, making it challenging to develop robust surrogate models. On queries poorly represented by the training set, data-driven predictive models risk producing non-physical artifacts, such as violations of conservation laws, causality, or symmetry. While transfer learning and multi-fidelity methods have emerged to alleviate data scarcity, ensuring physically consistent generalization remains a significant

challenge. Towards addressing this gap, current research increasingly emphasizes the development of PDE foundation models designed to achieve robust and unified generalization across diverse physical scenarios (Sun et al. 2025; Ye et al. 2024; Herde et al. 2024; Subramanian et al. 2023). Contemporary PDE surrogates employ a variety of architectures, from UNets (Ronneberger, Fischer, and Brox 2015), Transformers (Vaswani et al. 2023; Liu et al. 2021; Dosovitskiy et al. 2021), and Fourier Neural Operators (Li et al. 2021) to DeepONets (Lu et al. 2021) and bespoke designs (Gregory et al. 2024; Shankar et al. 2023), yet there is no consensus on which model class is most capable at scale. One must balance ease of optimization with the incorporation of physics priors, but quantitative tools for comparing loss-landscape properties across these architectures remain under-explored.

Insight into surrogate model behavior beyond static accuracy metrics can be gained through analysis of the model gradients. Examining gradients provides more accurate interpolation of prediction errors across the underlying data manifold; for instance, PINNs can be certified with continuous-domain error bounds (Eiras et al. 2024). By quantifying gradient overlap among different training examples, it is possible to identify potential conflicts or synergies in learned features. Precisely how gradients derived from individual training samples propagate through model parameters is formalized through the use of influence functions (Hampel 1974; Cook and Weisberg 1982). Influence functions were originally developed in robust statistics (Huber and Ronchetti 2009) to quantify how small perturbations of a data point in the training set affect model parameter estimations; their adaptation to deep networks provides insight into leave-one-out effects that do not require models to be re-trained on datasets with single examples excluded (Koh and Liang 2020; Bae et al. 2022). Diagonal elements of the influence function measure each training example’s leverage on its own prediction, high leverage points thereby identifying data that exerts disproportionate impact during training.

For PDE surrogate models, the influence framework can also pinpoint examples providing gradient signals that exacerbate violations of physical constraints (Naujoks et al. 2024). Furthermore, influence functions reveal spatio-temporal correlations inherent in PDE surrogate learning, distinguishing between memorization and genuine generalization in cases where the underlying solution operator lacks explicit space-time dependence, in addition to exposing gradient misalignments across distinct initial conditions (Wang et al. 2025) and inputs that are well separated in feature space. When applied to PDE foundation models, these techniques systematically characterize model stability, generalization capability, and uncertainty under realistic domain shifts and multi-physics scenarios, in addition to uncovering subtle failure modes typically missed by conventional evaluation metrics, thereby enabling targeted refinements of model, architecture, and training routines that yield more robust, physically-consistent, data-driven models (Ren et al. 2019; Zhang and Pfister 2021).

2 Related Work

Influence functions are powerful tools for understanding model behavior and data importance (Koh and Liang 2020; Bae et al. 2022). Robust and interpretable criteria for detecting anomalous inputs follow from techniques that analyze the alignment of gradients (Wang et al. 2025) by quantifying directional consistency with in-distribution data (Huang, Geng, and Li 2021), employ orthogonal projection (Behpour et al. 2023) to isolate anomalous components, and outlier gradient analysis (Chhabra et al. 2025).

Fort et al. (Fort et al. 2020) define stiffness in terms of the dot-product between the loss-gradients of two inputs. A positive stiffness then means that a stochastic gradient descent (SGD) step benefiting one example simultaneously lowers the loss of the other - evidence that the network assimilated shared, transferable features. Two summary statistics: sign-stiffness and cosine-stiffness, emphasize inter-class and intra-class correlations, respectively. Plotting stiffness against input-space distance yields a dynamic correlation length - the distance where average stiffness first crosses zero - which shrinks over epochs, revealing how the learned function becomes progressively more localized as specialization sets in.

The Coherent Gradients Hypothesis (Chatterjee 2020) proposed that per-example gradients tend to align for similar inputs, so SGD steps amplify directions supported by many examples while suppressing idiosyncratic ones, steering the network toward functions that generalize rather than memorize. Extensions of the Coherent Gradients Hypothesis (Zielinski, Krishnan, and Chatterjee 2020) posit that SGD updates aligned across multiple training examples (“strong” directions) underpin generalization, whereas idiosyncratic (“weak”) directions promote memorization. They introduce optimizers that suppress weak directions without computing per-example gradients, dramatically reducing the train-test gap-even in the presence of heavy label noise-and thereby offer the first large-scale confirmation of the hypothesis. Complementing this view, He and Su (He and Su 2020) establish the notion of local elasticity: in some neural networks, a parameter update perturbs predictions only within a narrow neighbourhood around the training point. PIN-Nfluence (Mlodozeniec et al. 2025) interrogates a trained physics-informed neural network under perturbations to the PDE parameters and reweighting of collocation points. They distill raw pointwise influences into physically meaningful diagnostics such as the Directional Indicator, which measures the fraction of influence that propagates downstream with the fluid flow, and the Region Indicator, which tallies influence concentrated in user-defined sub-domains.

3 Our Contributions

We make four key advances toward principled analysis and validation of PDE surrogate models:

1. **Time-aware analysis of off-diagonal influence function elements:** A systematic study off-diagonal influence function elements for PDE surrogate models, capable of quantifying training-sample leverage across physical time. This diagnostic sets standards for identifying the

learning of persistent nontrivial correlations that extend across temporal horizons, thereby identifying when the surrogate network has internalized fundamental, time-invariant PDE structures.

2. **Gradient-coherence diagnostics across initial condition classes:** Additionally, we determine the degree of alignment of gradients computed across different classes of PDE solutions for two standard architectures, a UNet and a ViT. Strong alignment signals the learning of robust, transferable physics, whereas weak alignment suggests that the neural network embeds these classes on separated regions of the input manifold, with limited gradient coherence, despite the fact that the data represents solutions to the same underlying PDE.
3. **Proximal Loss Landscape Geometry:** Our analysis demonstrates the computational feasibility of computing gradient overlap and influence within a proximal geometry setting, wherein the Riemannian metric is defined by the neural tangent kernel, thereby enabling the capture of intrinsic, non-Euclidean structure.
4. **Compact, invariant summaries via irreducible-representation decomposition:** Furthermore, this work introduces irreducible representations to facilitate a comprehensive analysis of linear response matrices that allows for the definition of multiple independent scalar quantities characteristic of gradient coherence.

4 Results

For the readers’ convenience, we provide the salient results of this work before specifying our training routine in Section 5 and providing mathematical details in Section 6.

Test-data measurements of the two-time influence function Equation 15 for both a UNet and a ViT exhibit rapid temporal decay in the off-diagonal terms [see Figure 1], which indicates that surrogate training constructs localized vector fields suitable only for interpolation within small neighborhoods of the training data sub-manifold, rather than the universally consistent function that is desired based on expectations stemming from our knowledge of the underlying governing equations. If such models were truly learning the solution operator to a PDE that lacks explicit time dependence, gradients derived from examples at a given time t would necessarily have a profound effect on the predictions at any other time τ , for we know that the true solution operator must take the same functional form at every point in phase space. Furthermore, there is a near-total absence of inter-class influence [see Figure 2]. We also visualize the negligible trust window horizon for initial condition examples [see Figure 3] and examples corresponding to a time-step in the wave-mixing regime [see Figure 4].

The alignment of gradients across examples also affords conclusions about the data manifold sparsity: while all inputs to the network are intimately related as unique solutions to a shared equation of motion under different initial conditions, the data manifold learned by both our ViT and our UNet render these points well separated in the sense that their gradients don’t meaningfully overlap unless the feature space distance between inputs is small [see Figure 5]. Such

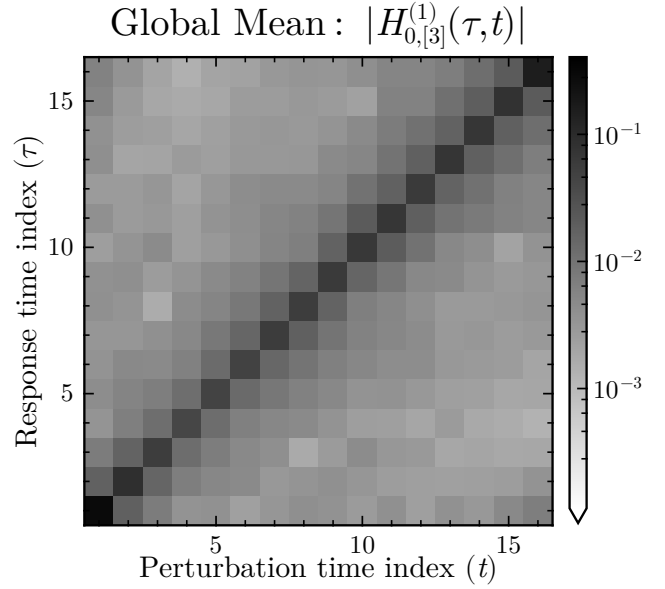


Figure 1: Sector norm of the overlap matrix between two loss gradients as a function of time separation for our UNet model. For a detailed definition of $H_{0,[3]}^{(1)}$, see Section 6.1 and Section 6.2.

results challenge a fundamental assumption motivating the development of PDE foundation models, as it demonstrates that these models are prone to effectively treating different classes of PDE solutions as distinct, isolated learning tasks. That this happens even when said classes of solutions arise merely from different initial conditions to the same physical process underscores the need for inductive biases to be explicitly incorporated during model development.

Even though our ViT outperformed our UNet on the in-distribution validation set [see Figure 7], its gradient structure is concerning. Indeed, our ViT shows a lower relative contribution to both the global mean and uniform background correlation components of the gradient overlap spectrum. It also displays greater variation beyond the isotropic level and a stronger tendency to decorrelate updates, even when gradients nominally align. These patterns suggest that our ViT relies on input-sensitive and class-specific representations, which reflects nonphysical fragmentation of the learned solution manifold. If the anti-symmetric contribution was significant, then one could expect a circulatory structure in those mini-batch gradients used for training.

In addition to the overlap of cost function gradients, we also considered gradients derived from physics informed loss functions [see Appendix D], such as global mass conservation [see Equation 16]. In all cases, we observed that the response function was dominated by its equal-time, intra-class, matrix elements. Hence, we conclude that predictive models lacking explicit inductive biases are not internalizing a unified governing law, but merely allocating parameters tasked specifically with evolving states associated with

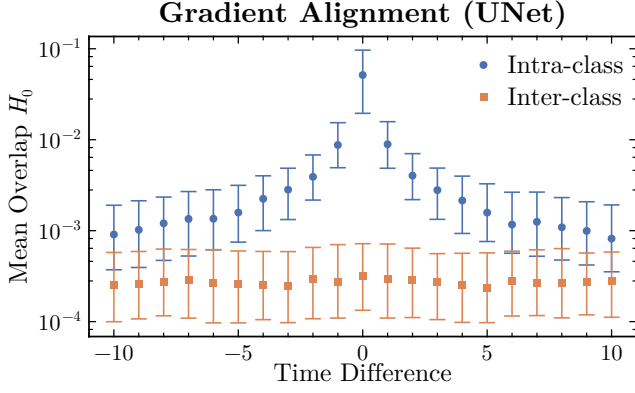


Figure 2: Average overlap of loss gradients as a function of time difference between their associated example inputs. By Inter-class, we indicate gradient overlap values between examples stemming from two different classes of initial conditions, whereas intra-class corresponds to overlap values within a given class of initial conditions.

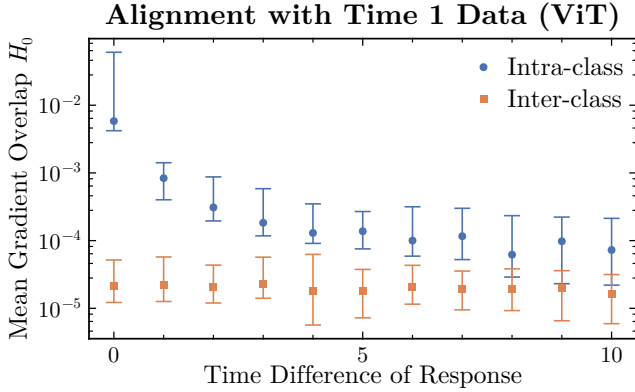


Figure 3: Values of overlap between gradients derived from initial condition examples and examples corresponding to a given time difference forward in the evolution.

a given time along a given class of trajectories. This superfluous time awareness presents across the entire training trajectory, demonstrating that the model did not learn the underlying solution operator.

5 Data and Training

We trained neural network surrogate models to approximate the evolution of two-dimensional compressible Euler flows, provided by the PDEGym dataset (Herde et al. 2024). Specifically, we used a dataset that contains three classes of initial conditions, namely, the four quadrant Riemann problem with (CE-RPUI) and without (CE-RP) uncertain interfaces, in addition to the curved Riemann problem (CE-CRP). These datasets are particularly valuable for studying the progression from a linear wave regime with discontinuities to fully developed turbulence, a crossover that poses computational and analytical challenges due to the presence

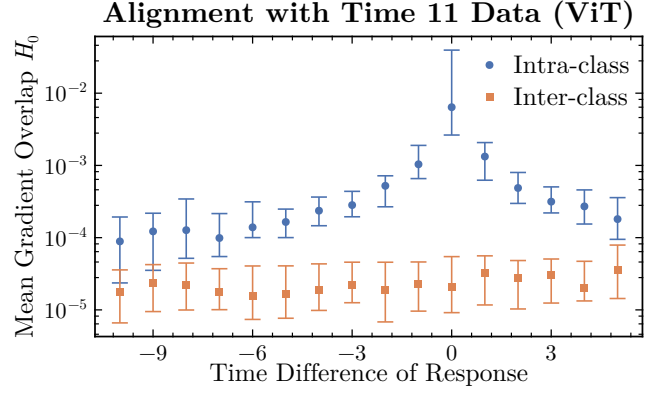


Figure 4: Values of overlap between gradients derived from examples at time 11 and examples corresponding to a given relative time difference in the evolution.

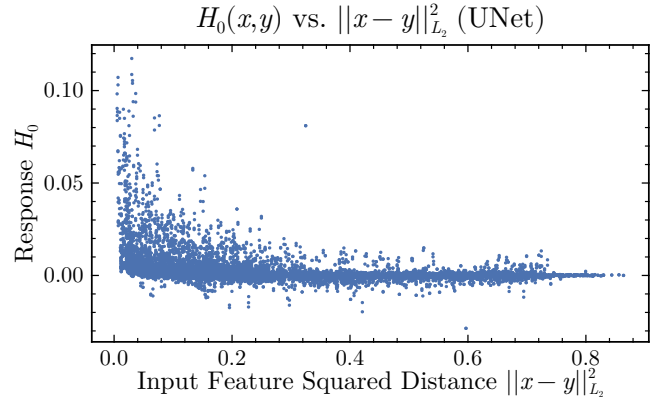


Figure 5: Values of loss gradient overlaps as a function of feature space difference between examples from which the gradients were derived.

of sharp wave-fronts and emergent nonlinear interactions. While the CE-RPUI, CE-RP, and CE-CRP datasets are all expected to exhibit comparable large-scale structures arising from Riemann-type initial conditions, they also display qualitatively distinct behaviors. In particular, CE-RPUI initial configurations give rise to complex finger-like instabilities in the flow field that are absent or less pronounced in both CE-RP and CE-CRP. In total, we used 5,000 trajectories for each of the three classes of initial conditions; for each trajectory, we used the first 16 time steps.

Since instantaneous flow states alone cannot distinguish viscous Navier–Stokes flows from their inviscid Euler counterparts, we used only the compressible Euler data. Furthermore, rather than representing a fluid state using the velocities and pressure in addition to density, as was done by Poseidon (Herde et al. 2024), we used the momentum and energy fields; we expect that this setup will facilitate the learning of all four conservation laws.

Each snapshot of the flow state at discrete time t is represented as a set of spatially discretized fields $\rho_{\text{mass}}, \rho_{\text{mom}}^i, \rho_{\text{energy}}$ on a uniform grid of size 128×128 ,

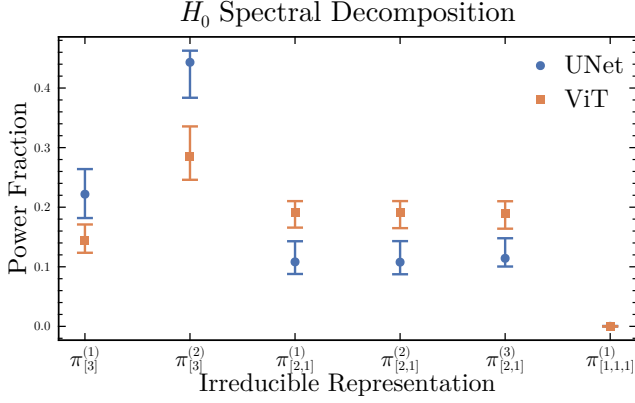


Figure 6: Per irreducible component percent contribution to the total SMSE gradient overlap matrix.

where ρ_{mass} denotes mass density, ρ_{mom}^i are the Cartesian components of momentum density, and ρ_{energy} is energy density. The model \hat{y}_θ is trained to emulate the compressible Euler evolution, i.e., $\hat{y}_\theta \approx U$, where the operator U enacts

$$s_{t+1} = U[s_t], \quad (1)$$

with s_t the collection of state variables at timestep t , via optimization of the weights θ . Specifically, we used the Adam optimizer (Kingma and Ba 2017) with learning rate 5×10^{-4} and weight decay $\lambda = 10^{-6}$ to minimize a scaled mean squared error (SMSE) between predicted and true states

$$C_{\text{SMSE}}(\theta) = \frac{1}{N} \sum_{n=1}^N \frac{1}{4} \sum_c \frac{\|\hat{y}_\theta^c(s_{t_n}) - s_{t_n+1}^c\|_{L_2}^2}{\text{RMS}(s_{t_n+1}^c)}, \quad (2)$$

on mini-batches containing $N = 64$ transitions $s_t \rightarrow s_{t+1}$, chosen randomly from the training set; here, the L_2 norm is computed over the spatial degrees of freedom and the channel index c runs through mass, both cartesian components of the momentum, and energy, respectively. $\text{RMS}(s^c)$ is computed channel-wise by taking the spatial root-mean-square of s^c . Thus, Equation 2 strikes a balance between ordinary and relative mean-squared-error; normalizing each channel’s squared error by the target fields’ characteristic amplitude favors examples containing pronounced features, but does not completely drown out gradients derived from relatively quiescent flows, thereby facilitating accurate capture of high-energy shocks and wavefronts without harsh under-emphasis of small-amplitude features. Moreover, the scaling of Equation 2 renders dimensionless the matrix elements of interest to this work.

In order to compare the results of our experiments across model architectures, we trained both a UNet (Ronneberger, Fischer, and Brox 2015) and a vision transformer (ViT) (Vaswani et al. 2023; Liu et al. 2021; Dosovitskiy et al. 2021). Our UNet was based on BigGAN (Brock, Donahue, and Simonyan 2019), with four down-sampling blocks and 24 channels after the initial embedding layer, for a total of about 13-million parameters. Our vision transformer was of layer-depth six, with 256 channels, for a total of about 5-million parameters, fewer than our UNet due to memory

constraints on the 40 GB A100s that we used for training. The training of each model was performed in distributed mode across two such A100s using Lux.jl (Pal 2023a,b), with Zygote.jl as our auto-differentiation backend (Innes 2018). Plots in this manuscript were generated using Makie.jl (Danisch and Krumbiegel 2021).

The validation losses for each of our models is shown in [see Figure 7]. Despite possessing fewer parameters, our ViT model consistently outperformed the UNet after 90 training epochs. Each of the two architectures was trained three times, sharing those three seeds that controlled initialization and dataset split.

Optimization Curve (Validation Data)

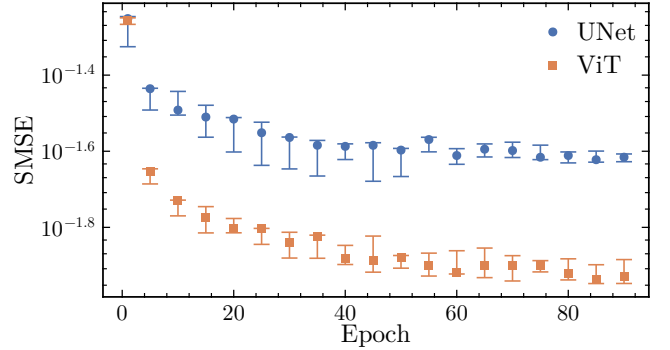


Figure 7: Median validation loss development during optimization with range bars indicating the range between the best and worst performance at each epoch.

6 Response Function

To understand how individual data points influence parameter estimation, we examine the sensitivity of the model to cost perturbations

$$C(\theta) \rightarrow C(\theta) + \delta L(\theta), \quad (3)$$

where $\delta L(\theta)$ is a small forcing term. By leaving δL momentarily unspecified, we capture the linear response structure for a wide range of influence diagnostics, including data reweighting and modification. Note that δL derives its model weight θ dependence through the model \hat{y}_θ evaluated on one or more training examples.

We take inspiration from (Bae et al. 2022) by defining the following proximal objective, with reference to the weights θ^* determined by Adam after 90 epochs of training,

$$S^{\theta^*}(\theta) = \langle \theta - \theta^*, \nabla C(\theta^*) \rangle_\eta + \|\hat{y}_\theta - \hat{y}_{\theta^*}\|_{L_2}^2 + \frac{\lambda}{2} \theta^2 \quad (4)$$

and consider the resulting change in optimal parameters

$$\delta \theta^* = -\chi \nabla \delta L, \quad (5)$$

where the inverse susceptibility tensor

$$\chi_{\alpha\beta}^{-1} = \lambda \delta_{\alpha\beta} + \eta_{\alpha\beta}, \quad (6)$$

serves as a generalized stiffness operator that relates an infinitesimal change in the gradient to a parameter displacement $\delta\theta^*$; here, the Riemann metric η is given by the neural tangent kernel

$$\eta_{\alpha\beta} = J_{\alpha}^n J_{\beta}^n. \quad (7)$$

Greek letters index trainable parameters θ_{α} , while the Roman letter n indexes individual examples $(s_{t_n}, s_{t_{n+1}})$. Contracting χ with the model Jacobian

$$J_{\alpha}^n = \partial_{\alpha} \hat{y}^n, \quad (8)$$

yields the output response to cost perturbations, i.e., δL induces a change in the predictions according to

$$\delta \hat{y}^n = -\Pi^{nm} \frac{\delta}{\delta \hat{y}^m} \delta L, \quad (9)$$

where the response function

$$\Pi^{nm} = J_{\alpha}^n \chi^{\alpha\beta} J_{\beta}^m. \quad (10)$$

To obtain the related expression familiar from classical influence function theory, develop

$$\delta L = \frac{\delta C}{\delta y} \delta y \quad (11)$$

and write

$$\frac{\delta \hat{y}^n}{\delta \hat{y}^m} = -\Pi^{nl} \frac{\delta^2 C}{\delta \hat{y}^l \delta \hat{y}^m}, \quad (12)$$

which is identically equal to Π when C is the mean squared error cost. Equation 11 allows for investigating the influence of both physics-informed and numerical-routine aware data modifications, which we save for future work. By formulating the mathematics as above, we emphasize that the proximal penalty in Equation 4 sets the geometry of the update and clearly identifies Π as the primary object controlling the model sensitivity to a general cost perturbation. Interpretation Π is available through analogy with concepts from statistics, machine learning, and physics.

In the limit of vanishing regularization, $\lambda \rightarrow 0$, Π becomes idempotent, assuming the form of a classical hat matrix. Consequently, we take the view that diagonal elements $n = m$ reflect statistical leverage, quantifying the self-influence of individual training examples, while off-diagonal elements $n \neq m$ measure cross-influence between distinct examples [see Figure 6]. High leverage scores identify regions of parameter space with strong local curvature or limited redundancy, i.e., points with disproportionately large influence on the global response structure [see Figure 1]. Furthermore, the response matrix encodes the pairwise overlap of example gradients-effectively probing the local loss landscape by highlighting directions of correlated curvature and shared descent paths [see Figure 5]. Physical considerations that guide expectations for the structure of Π are evident on recognizing that we have so far suppressed the feature indices in the model Jacobian. The response matrix tracks how gradients derived from each output feature of prediction m influence each output feature of prediction n , offering an investigative level of detail across spacetime and channel dimensions that remains unexplored [see Figure 2].

6.1 Matrix Elements of Π

Our objective is to determine to what extent an infinitesimal perturbation in the either the cost functional or input data propagates to an observable, such as the mean squared error or physical consistency of predictions. Because each flow field has $128 \times 128 \times 4$ degrees of freedom, together with the large number of trainable parameters in our models, a direct inversion to determine χ is not computationally possible. Instead, we apply an iterative matrix-free solver, specifically the CRAIG method (Orban and Arioli 2017) provided by the Krylov.jl package (Montoison and Orban 2023), which is formally equivalent to conjugate gradient descent, to efficiently approximate the required sensitivities. While this approach does not leverage commonly used scalable approximations (George 2021; TransferLab 2024), we have control over the iterative solver error through a relative tolerance parameter. When evaluating our UNet models, we determine the action of χ with a relative error tolerance of 5×10^{-3} ; for reasons of computation time, we use a relative tolerance of 5×10^{-2} for our ViT models. Moreover, to avoid materializing the entire response matrix, we selectively evaluate only those matrix elements corresponding to physically or statistically meaningful couplings.

Matrix elements of Π were determined for three distinct mini-batches, each of which contained three trajectories corresponding to distinct initial conditions, for each seed of each model architecture trained. An average over the resulting nine mini-batches was computed after scaling each response matrix to be of unit norm, otherwise mini-batches with examples of large residual are overly represented.

Cost Perturbations Our probe of generalization capabilities proceeds by quantifying the coherence of gradients derived from test data. To this end, we introduce two conjugate forces

$$r_{\text{SMSE}}^c = \frac{\delta}{\delta \hat{y}_{\theta}^c} \delta C_{\text{SMSE}} = \frac{\hat{y}_{\theta}^c - y^c}{\text{RMS}(y^c)} \quad (13)$$

and

$$r_{\text{Mass}} = \frac{\delta}{\delta \hat{y}_{\theta}} \delta C_{\text{Mass}} = \frac{M[\hat{y}_{\theta}] - M[x]}{M[x]}, \quad (14)$$

where $M[\cdot]$ computes the total mass of its argument, x is the input state that evolves to y , i.e. $y = U[x]$, where U is defined in Equation 1, and \hat{y} is the neural network approximation to y . Recall that each training example is comprised of pairs $(x, y) = (s_t^n, s_{t+1}^n)$ of states s sharing a common initial configuration indexed by n , and related by the compressible Euler evolution operator.

Viewed as a coupling matrix over generalized forces, the diagonal blocks of Π recover the usual influence (e.g., how a perturbation in the SMSE affects SMSE itself), while the off-diagonal blocks encode cross-coupling, quantifying how a change in the SMSE residual at one time step or sample is converted into the conservation residual at another time step or sample, and vice versa.

It is useful to introduce following notation for the remaining external indices of the response matrix

$$H(t, n | \tau, m) = (r_t^n, \Pi_{t\tau}^{nm} r_{\tau}^m), \quad (15)$$

where n, m index trajectories, defined by distinct initial conditions, and t, τ index the time step along said trajectories. Furthermore, we define

$$H_0 = (r_{\text{SMSE}}, \Pi r_{\text{SMSE}}), \quad (16a)$$

$$H_1 = (r_{\text{SMSE}}, \Pi r_{\text{Mass}}), \quad (16b)$$

$$H_2 = (r_{\text{Mass}}, \Pi r_{\text{Mass}}), \quad (16c)$$

in order to facilitate discussion of the full response matrix over generalized forces. H_0 gives the change in SMSE due to an SMSE perturbation, while H_1 and H_2 propagate the effect of gradients derived from the physics informed mass conservation loss into the SMSE and mass conservation error, respectively.

6.2 Irreducible Representations

It is natural to decompose the space our hat matrices into irreducible representations of S_3 , the symmetric group on three letters. This decomposition is performed at each time pair t, τ , for the relevant symmetry group on the time indices is the translation group.

We view linear maps $M : \mathbb{R}^3 \rightarrow \mathbb{R}^3$, such as H in Equation 15, as rank-2 tensors that transform under the symmetric group S_3 . It is well known that any $M \in \text{End}(\mathbb{R}^3)$ can be expressed (Fulton and Harris 1991)

$$M = M_{[3]}^{(1)} + M_{[3]}^{(2)} + M_{[1,1,1]}^{(1)} + M_{[2,1]}^{(1)} + M_{[2,1]}^{(2)} + M_{[2,1]}^{(3)} \quad (17)$$

where the blocks $M_{\lambda}^{(k)}$ are defined in Appendix B. Here, summands of subscript λ denote subspaces of endomorphisms transforming according to the irreducible of shape λ . That the projections onto distinct irreducible sectors are pairwise orthogonal facilitates a comprehensive and invariant overview of how each irreducible sector contributes to M . The components $M_{\lambda}^{(k)}$ admit the following interpretations:

Global mean: $M_{[3]}^{(1)}$ equals the outer product of the average gradient with itself and records the common direction shared by all examples.

Diagonal bias $M_{[3]}^{(2)}$ represents uniform background correlations that remain after row and column means have been removed.

Directional skew: $M_{[1,1,1]}^{(1)}$ the anti-symmetry components, record non-reciprocal influence.

Row bias: $M_{[2,1]}^{(1)}$ measures how strongly each example aligns with the mean gradient. Large positive (negative) entries indicate over-alignment (anti-alignment) relative to the average.

Column bias: $M_{[2,1]}^{(2)}$ quantifies how strongly each column aligns or anti-aligns with the overall mean, with large (small) values indicating systematic over (under) influence. Coincides with the row bias when M is symmetric.

Residual Overlap: $M_{[2,1]}^{(3)}$ captures variation in the overlaps across examples once the isotropic level has been subtracted.

7 Conclusion

Our research reveals a critical shortcoming common to physics-agnostic PDE surrogates: it is not an immediate consequence of large-scale multi-scenario training that the resulting trained model can satisfy those stringent expectations that follow from the governing equations one is trying to emulate. This mismatch underscores the importance of enforcing principled physics-based constraints, either as weak regularizers during training, or baked in strictly through architectural design. By measuring gradient overlap between classes of initial conditions we reveal an absence of coherent gradients, which suggests limited learning of robust, transferable physics. This demonstrates that both the ViT and UNet surrogates embed these solution classes on nearly disjoint manifolds challenges the efficacy of current multi-scenario training pipelines.

We demonstrate that influence functions form a versatile diagnostic framework and demonstrate their effectiveness in revealing the degree of balance between memorization and generalization in autoregressive predictors [see Figure 8]. Our analysis suggests that ordinary data-driven PDE surro-

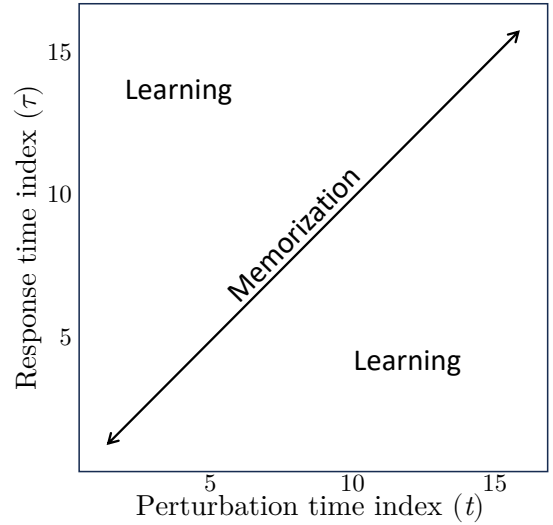


Figure 8: Schematic indicating the learning and memorization regimes of the two-time influence function.

gates behave as statistical estimators, producing predictions primarily based on those training examples that lie within a neighborhood of the input query. While this localized learning mechanism provides resilience against noisy data, it also restricts generalization, and indicates that the learned data manifold geometry is composed of largely isolated regions.

In summary, we highlight a new, concrete, and targetable characteristics to guide researchers in designing algorithms capable of learning the underlying generative process and achieving reliable long-term rollouts.

Acknowledgments. Research presented in this report was supported by the Laboratory Directed Research and Development program of Los Alamos National Laboratory under project number(s) 20250637DI, 20250638DI, and 20250639DI. This research used resources provided by the Los Alamos National Laboratory Institutional Computing Program, which is supported by the U.S. Department of Energy National Nuclear Security Administration under Contract No. 89233218CNA000001. It is published under LA-UR-25-28084.

References

- Amari, S.-i. 1998. Natural Gradient Works Efficiently in Learning. *Neural Computation*, 10(2): 251–276.
- Bae, J.; Ng, N.; Lo, A.; Ghassemi, M.; and Grosse, R. 2022. If Influence Functions are the Answer, Then What is the Question? arXiv:2209.05364.
- Batatia, I.; Benner, P.; Chiang, Y.; Elena, A. M.; Kovács, D. P.; Riebesell, J.; Advincula, X. R.; Asta, M.; Avaylon, M.; Baldwin, W. J.; Berger, F.; Bernstein, N.; Bhowmik, A.; Blau, S. M.; Cărare, V.; Darby, J. P.; De, S.; Pia, F. D.; Deringer, V. L.; Elijošius, R.; El-Machachi, Z.; Falcioni, F.; Fako, E.; Ferrari, A. C.; Genreith-Schriever, A.; George, J.; Goodall, R. E. A.; Grey, C. P.; Grigorev, P.; Han, S.; Handley, W.; Heenen, H. H.; Hermansson, K.; Holm, C.; Jaafar, J.; Hofmann, S.; Jakob, K. S.; Jung, H.; Kapil, V.; Kaplan, A. D.; Karimitari, N.; Kermode, J. R.; Kroupa, N.; Kullgren, J.; Kuner, M. C.; Kuryla, D.; Liepuoniute, G.; Margraf, J. T.; Magdău, I.-B.; Michaelides, A.; Moore, J. H.; Naik, A. A.; Niblett, S. P.; Norwood, S. W.; O’Neill, N.; Ortner, C.; Persson, K. A.; Reuter, K.; Rosen, A. S.; Schaaf, L. L.; Schran, C.; Shi, B. X.; Sivonxay, E.; Stenczel, T. K.; Svahn, V.; Sutton, C.; Swinburne, T. D.; Tilly, J.; van der Oord, C.; Varga-Umbrich, E.; Vegge, T.; Vondrák, M.; Wang, Y.; Witt, W. C.; Zills, F.; and Csányi, G. 2024. A foundation model for atomistic materials chemistry. arXiv:2401.00096.
- Behpour, S.; Doan, T.; Li, X.; He, W.; Gou, L.; and Ren, L. 2023. GradOrth: A Simple yet Efficient Out-of-Distribution Detection with Orthogonal Projection of Gradients. arXiv:2308.00310.
- Bodnar, C.; Bruinsma, W. P.; Lucic, A.; Stanley, M.; Vaughan, A.; Brandstetter, J.; Garvan, P.; Riechert, M.; Weyn, J. A.; Dong, H.; Gupta, J. K.; Thambiratnam, K.; Archibald, A. T.; Wu, C.-C.; Heider, E.; Welling, M.; Turner, R. E.; and Perdikaris, P. 2024. A Foundation Model for the Earth System. arXiv:2405.13063.
- Brandstetter, J.; Worrall, D.; and Welling, M. 2023. Message Passing Neural PDE Solvers. arXiv:2202.03376.
- Brock, A.; Donahue, J.; and Simonyan, K. 2019. Large Scale GAN Training for High Fidelity Natural Image Synthesis. arXiv:1809.11096.
- Chatterjee, S. 2020. Coherent Gradients: An Approach to Understanding Generalization in Gradient Descent-based Optimization. arXiv:2002.10657.
- Chatterjee, S.; and Zielinski, P. 2022. On the Generalization Mystery in Deep Learning. arXiv:2203.10036.
- Chhabra, A.; Li, B.; Chen, J.; Mohapatra, P.; and Liu, H. 2025. Outlier Gradient Analysis: Efficiently Identifying Detrimental Training Samples for Deep Learning Models. In *Forty-second International Conference on Machine Learning*.
- Cook, R. D.; and Weisberg, S. 1982. *Residuals and Influence in Regression*. New York: Chapman and Hall. ISBN 0-412-24280-0.
- Danisch, S.; and Krumbiegel, J. 2021. Makie.jl: Flexible high-performance data visualization for Julia. *Journal of Open Source Software*, 6(65): 3349.
- Dosovitskiy, A.; Beyer, L.; Kolesnikov, A.; Weissenborn, D.; Zhai, X.; Unterthiner, T.; Dehghani, M.; Minderer, M.; Heigold, G.; Gelly, S.; Uszkoreit, J.; and Houlsby, N. 2021. An Image is Worth 16x16 Words: Transformers for Image Recognition at Scale. arXiv:2010.11929.
- Eiras, F.; Bibi, A.; Bunel, R.; Dvijotham, K. D.; Torr, P.; and Kumar, M. P. 2024. Efficient Error Certification for Physics-Informed Neural Networks. arXiv:2305.10157.
- Foret, P.; Kleiner, A.; Mobahi, H.; and Neyshabur, B. 2021. Sharpness-Aware Minimization for Efficiently Improving Generalization. arXiv:2010.01412.
- Fort, S.; Nowak, P. K.; Jastrzebski, S.; and Narayanan, S. 2020. Stiffness: A New Perspective on Generalization in Neural Networks. arXiv:1901.09491.
- Fulton, W.; and Harris, J. 1991. *Representation Theory*. New York, NY: Springer Science. ISBN 978-1-4612-0979-9.
- George, T. 2021. NNGeometry: Easy and Fast Fisher Information Matrices and Neural Tangent Kernels in PyTorch.
- Gregory, W. G.; Hogg, D. W.; Blum-Smith, B.; Arias, M. T.; Wong, K. W. K.; and Villar, S. 2024. Equivariant geometric convolutions for emulation of dynamical systems. arXiv:2305.12585.
- Gupta, J. K.; and Brandstetter, J. 2022. Towards Multi-spatiotemporal-scale Generalized PDE Modeling. arXiv:2209.15616.
- Guzmán-Cordero, A.; Dangel, F.; Goldshlager, G.; and Zeinhofer, M. 2025. Improving Energy Natural Gradient Descent through Woodbury, Momentum, and Randomization. arXiv:2505.12149.
- Hampel, F. R. 1974. The Influence Curve and its Role in Robust Estimation. *Journal of the American Statistical Association*, 69(346): 383–393.
- He, H.; and Su, W. J. 2020. The Local Elasticity of Neural Networks. arXiv:1910.06943.
- Herde, M.; Raonić, B.; Rohner, T.; Käppeli, R.; Molinaro, R.; de Bézenac, E.; and Mishra, S. 2024. Poseidon: Efficient Foundation Models for PDEs. arXiv:2405.19101.
- Huang, R.; Geng, A.; and Li, Y. 2021. On the Importance of Gradients for Detecting Distributional Shifts in the Wild. arXiv:2110.00218.
- Huber, P. J.; and Ronchetti, E. M. 2009. *Robust Statistics*. Wiley Series in Probability and Statistics. John Wiley & Sons, Inc. ISBN 9780470129906.
- Innes, M. 2018. Don’t Unroll Adjoint: Differentiating SSA-Form Programs. *CoRR*, abs/1810.07951.

- Jacot, A.; Gabriel, F.; and Hongler, C. 2020. Neural Tangent Kernel: Convergence and Generalization in Neural Networks. *arXiv:1806.07572*.
- Karniadakis, G.; Bilonis, I.; and Perdikaris, P. 2021. Physics-Informed Machine Learning. *Nature Reviews Physics*, 3: 422–440.
- Kingma, D. P.; and Ba, J. 2017. Adam: A Method for Stochastic Optimization. *arXiv:1412.6980*.
- Koh, P. W.; and Liang, P. 2020. Understanding Black-box Predictions via Influence Functions. *arXiv:1703.04730*.
- Krishnapriyan, A. S.; Gholami, A.; Zhe, S.; Kirby, R. M.; and Mahoney, M. W. 2021. Characterizing possible failure modes in physics-informed neural networks. *arXiv:2109.01050*.
- Lee, Y. 2023. Autoregressive Renaissance in Neural PDE Solvers. In *ICLR Blogposts 2023*.
- Li, Z.; Kovachki, N.; Azizzadenesheli, K.; Liu, B.; Bhattacharya, K.; Stuart, A.; and Anandkumar, A. 2021. Fourier Neural Operator for Parametric Partial Differential Equations. *arXiv:2010.08895*.
- Lippe, P.; Veeling, B. S.; Perdikaris, P.; Turner, R. E.; and Brandstetter, J. 2023. PDE-Refiner: Achieving Accurate Long Rollouts with Neural PDE Solvers. *arXiv:2308.05732*.
- Liu, Z.; Lin, Y.; Cao, Y.; Hu, H.; Wei, Y.; Zhang, Z.; Lin, S.; and Guo, B. 2021. Swin Transformer: Hierarchical Vision Transformer using Shifted Windows. *arXiv:2103.14030*.
- Lu, L.; Jin, P.; Pang, G.; Zhang, Z.; and Karniadakis, G. E. 2021. Learning nonlinear operators via DeepONet based on the universal approximation theorem of operators. *Nature Machine Intelligence*, 3(3): 218–229.
- Martens, J. 2020. New Insights and Perspectives on the Natural Gradient Method. *Journal of Machine Learning Research*, 21(146): 1–76.
- Mlodozieniec, B.; Eschenhagen, R.; Bae, J.; Immer, A.; Krueger, D.; and Turner, R. 2025. Influence Functions for Scalable Data Attribution in Diffusion Models. *arXiv:2410.13850*.
- Montoison, A.; and Orban, D. 2023. Krylov.jl: A Julia basket of hand-picked Krylov methods. *Journal of Open Source Software*, 8(89): 5187.
- Müller, J.; and Zeinhofer, M. 2023. Achieving High Accuracy with PINNs via Energy Natural Gradients. *arXiv:2302.13163*.
- Naujoks, J. R.; Krasowski, A.; Weckbecker, M.; Wiegand, T.; Lapuschkin, S.; Samek, W.; and Klausen, R. P. 2024. PINNfluence: Influence Functions for Physics-Informed Neural Networks. *arXiv:2409.08958*.
- Ohana, R.; McCabe, M.; Meyer, L.; Morel, R.; Agocs, F. J.; Beneitez, M.; Berger, M.; Burkhart, B.; Burns, K.; Dalziel, S. B.; Fielding, D. B.; Fortunato, D.; Goldberg, J. A.; Hirashima, K.; Jiang, Y.-F.; Kerswell, R. R.; Maddu, S.; Miller, J.; Mukhopadhyay, P.; Nixon, S. S.; Shen, J.; Watteaux, R.; Blancard, B. R.-S.; Rozet, F.; Parker, L. H.; Cranmer, M.; and Ho, S. 2025. The Well: a Large-Scale Collection of Diverse Physics Simulations for Machine Learning. *arXiv:2412.00568*.
- Orban, D.; and Arioli, M. 2017. *Iterative Solution of Symmetric Quasi-Definite Linear Systems*. Philadelphia, PA: Society for Industrial and Applied Mathematics.
- Pal, A. 2023a. Lux: Explicit Parameterization of Deep Neural Networks in Julia.
- Pal, A. 2023b. On Efficient Training & Inference of Neural Differential Equations.
- Picot, M.; Messina, F.; Boudiaf, M.; Labeau, F.; Ayed, I. B.; and Piantanida, P. 2023. Adversarial Robustness Via Fisher-Rao Regularization. *IEEE Transactions on Pattern Analysis and Machine Intelligence*, 45(3): 2698–2710.
- Raissi, M.; Perdikaris, P.; and Karniadakis, G. 2019. Physics-informed neural networks: A deep learning framework for solving forward and inverse problems involving nonlinear partial differential equations. *Journal of Computational Physics*, 378: 686–707.
- Ren, M.; Zeng, W.; Yang, B.; and Urtasun, R. 2019. Learning to Reweight Examples for Robust Deep Learning. *arXiv:1803.09050*.
- Ronneberger, O.; Fischer, P.; and Brox, T. 2015. U-Net: Convolutional Networks for Biomedical Image Segmentation. *arXiv:1505.04597*.
- Shankar, V.; Barwey, S.; Kolter, Z.; Maulik, R.; and Viswanathan, V. 2023. Importance of equivariant and invariant symmetries for fluid flow modeling. *arXiv:2307.05486*.
- Subramanian, S.; Harrington, P.; Keutzer, K.; Bhimji, W.; Morozov, D.; Mahoney, M.; and Gholami, A. 2023. Towards Foundation Models for Scientific Machine Learning: Characterizing Scaling and Transfer Behavior. *arXiv:2306.00258*.
- Sun, J.; Liu, Y.; Zhang, Z.; and Schaeffer, H. 2025. Towards a Foundation Model for Partial Differential Equations: Multi-Operator Learning and Extrapolation. *arXiv:2404.12355*.
- Takamoto, M.; Praditia, T.; Leiteritz, R.; MacKinlay, D.; Alesiani, F.; Pflüger, D.; and Niepert, M. 2024. PDEBENCH: An Extensive Benchmark for Scientific Machine Learning. *arXiv:2210.07182*.
- TransferLab. 2024. pyDVL.
- Vaswani, A.; Shazeer, N.; Parmar, N.; Uszkoreit, J.; Jones, L.; Gomez, A. N.; Kaiser, L.; and Polosukhin, I. 2023. Attention Is All You Need. *arXiv:1706.03762*.
- Wang, S.; Bhartari, A. K.; Li, B.; and Perdikaris, P. 2025. Gradient Alignment in Physics-informed Neural Networks: A Second-Order Optimization Perspective. *arXiv:2502.00604*.
- Ye, Z.; Huang, X.; Chen, L.; Liu, H.; Wang, Z.; and Dong, B. 2024. PDEformer: Towards a Foundation Model for One-Dimensional Partial Differential Equations. In *ICLR 2024 Workshop on AI4DifferentialEquations In Science*.
- Zhang, Z.; and Pfister, T. 2021. Learning Fast Sample Reweighting Without Reward Data. *arXiv:2109.03216*.
- Zielinski, P.; Krishnan, S.; and Chatterjee, S. 2020. Weak and Strong Gradient Directions: Explaining Memorization, Generalization, and Hardness of Examples at Scale. *arXiv:2003.07422*.

A Linear Response

In this section we develop the linear response framework for physics-informed PDE surrogates. This framework provides a unified diagnostic tool to probe model behavior under domain shifts, quantify the impact of individual training examples, reveal temporal correlations, and expose gradient misalignments across classes of initial conditions. Provided by their sensitivity to the underlying loss landscape geometry, these linear response diagnostics can uncover subtle failure modes missed by static evaluation metrics, guide targeted refinements, and support the systematic evaluation of stability, generalization, and uncertainty in scientific machine learning.

Let $\theta, \phi \in \mathbb{R}^p$ denote two elements of parameter space. On this space, define an inner product

$$\langle \varphi, \phi \rangle_\eta = \varphi^\alpha \eta_{\alpha\beta} \phi^\beta, \quad (18)$$

where $\eta_{\alpha\beta}$ is the metric tensor. Throughout this work, repeated indices are to be summed over under the Einstein convention unless stated otherwise.

In this formulation, learning proceeds by updating parameters θ through a sequence of local variational problems. With reference to a point θ_0 , we define the action

$$S^{\theta_0}(\theta) = \langle \theta - \theta_0, \nabla C(\theta_0) \rangle_\eta + D^{\theta_0}(\theta) + R(\theta), \quad (19)$$

where $C : \mathbb{R}^p \rightarrow \mathbb{R}$ is the cost function, $D^{\theta_0} : \mathbb{R}^p \rightarrow \mathbb{R}$ is a divergence that penalizes departure of θ from θ_0 , and $R : \mathbb{R}^p \rightarrow \mathbb{R}$ encodes regularization or prior structure. The parameters are updated via the proximal rule

$$\theta_{k+1} = \arg \min_{\theta} S^{\theta_k}(\theta), \quad (20)$$

with each iteration refining the estimate by minimizing the local objective Equation 18.

The first term in Equation 19 represents the linear drift induced by the local gradient of the cost. The divergence D acts as a kinetic term that restrains motion and sets the geometry of the update. For our point-predictor \hat{y}_θ , we will use proximity in function space

$$D_{\text{NTK}}^{\theta_0}(\theta) = \frac{1}{2} (\hat{y}_\theta - \hat{y}_{\theta_0}, \hat{y}_\theta - \hat{y}_{\theta_0}), \quad (21)$$

where (\cdot, \cdot) is the Euclidean inner product on feature space. Equation 21 treats model predictions as primary and directly penalizes changes in the output, thereby encouraging a smooth evolution in feature space according to the manifold induced by the network. The natural choice in metric is the local curvature of D , in our case, the NTK metric (Jacot, Gabriel, and Hongler 2020)

$$\eta_{\alpha\beta}^{\text{NTK}}(\theta) = (\partial_\alpha \hat{y}_\theta) (\partial_\beta \hat{y}_\theta), \quad (22)$$

which measures how parameter perturbations change model outputs and therefore encodes the function-space sensitivity set by the network architecture and data. This construction mirrors Amari’s Fisher-Rao metric (Amari 1998), where the Fisher information matrix endows the parameter manifold with a Riemannian geometry defined by the sensitivity of the output distribution to infinitesimal parameter shifts. Just

as the Fisher metric underlies the natural gradient, providing more efficient (Guzmán-Cordero et al. 2025; Müller and Zeinhofer 2023) and robust (Picot et al. 2023) training by following the steepest descent in information space (Martens 2020), the NTK metric reveals intrinsic distances in function space, offering a principled means of analyzing generalization (Foret et al. 2021) and stability in PDE surrogates. On making the empirical Fisher approximation, the NTK metric can also be obtained by specializing the generalized Gauss-Newton matrix to the case of cost functions quadratic in the model.

For the regularization term R we take a ridge penalty of the form

$$R(\theta) = \frac{\lambda}{2} \langle \theta, \theta \rangle_\eta. \quad (23)$$

To understand how individual data points influence parameter estimation, we examine the sensitivity of the proximal update θ^* to small perturbations of the cost

$$C(\theta) \rightarrow C(\theta) + \delta L(\theta), \quad (24)$$

where $\delta L(\theta)$ is a small forcing term. By leaving δL momentarily unspecified, we capture the linear response structure for a wide range of influence diagnostics, including data reweighting and modification. Note that δL derives its θ dependence implicitly through the model \hat{y}_θ evaluated on one or more training examples. This formulation provides a flexible framework for analyzing how localized changes in the loss influence the model’s learned parameters.

Let θ^* denote the solution of the proximal variational problem Equation 19, and introduce the susceptibility tensor χ as the first variational coefficient

$$\delta \theta^* = -\chi \delta g, \quad (25)$$

where the gradient variation

$$\delta g = \nabla \delta L. \quad (26)$$

On restricting our analysis to nearly converged models and assuming that residual gradients g are small, it follows that

$$\chi_{\alpha\beta}^{-1}(\theta^*) = \partial_\alpha \partial_\beta [D^{\theta_0}(\theta^*) + R(\theta^*)]. \quad (27)$$

The inverse susceptibility tensor χ^{-1} serves as a generalized stiffness operator that relates an infinitesimal change in the gradient δg to a parameter displacement $\delta \theta^*$. Contracting χ with the model Jacobian $J_\alpha^n = \partial_\alpha f^n$, where n indexes a training example, yields the output response to cost perturbations, i.e., δL induces a change in the predictions according to

$$\delta \hat{y}^n = -\Pi^{nm} \frac{\delta}{\delta \hat{y}^m} \delta L, \quad (28)$$

where the response function

$$\Pi^{nm} = J_\alpha^n \chi^{\alpha\beta} J_\beta^m. \quad (29)$$

It is useful to introduce additional notation: let

$$r = \frac{\delta}{\delta \hat{y}} L \quad (30)$$

be the generalized force derived from δL and consider the cost function response

$$H^{nm} = \delta C^{nm} = (r^n, \Pi^{nm} r^m), \quad (31)$$

where the indices n, m are not subject to Einstein summation. Evidently, our goal is to calculate particular matrix elements of the response function.

B Irreducible Representations of the Symmetric Group

Consider the symmetric group S_n acting on $V = \mathbb{R}^n$, and let e_1, \dots, e_n be the standard basis. Define the vector $u \in V$ by its components Let

$$u = \frac{1}{\sqrt{n}} \sum_{j=1}^n e_j \quad (32)$$

be a basis element of

$$U = \{\alpha u \mid \alpha \in \mathbb{R}\}, \quad (33)$$

the trivial representation of S_n . With respect to the standard inner product on V , which we denote by $v_1 \cdot v_2$ for any two vectors $v_1, v_2 \in V$, the orthogonal complement of U

$$W = \{w \in \mathbb{R}^n \mid w \cdot u = 0\} \quad (34)$$

is an $(n-1)$ -dimensional invariant subspace carrying the standard representation of S_n . This orthogonal decomposition

$$V = U \oplus W \quad (35)$$

is more conveniently expressed in a manner that tracks irreducible types using partition notation

$$V \cong [n] \oplus [n-1, 1], \quad (36)$$

where the trivial representation corresponds to the partition $[n]$ and the standard representation corresponds to the partition $[n-1, 1]$. The purpose of this section is to realize such a complete irreducible decomposition for the space of endomorphisms on V , viz.

$$\begin{aligned} \text{End}(\mathbb{R}^n) \cong & 2[n] \oplus 3[n-1, 1] \\ & \oplus [n-2, 2] \oplus [n-2, 1, 1]. \end{aligned} \quad (37)$$

Here, summands of subscript λ denote the subspace of endomorphisms transforming according to the irreducible of shape λ with multiplicity given by their coefficient. Concretely, any $M \in \text{End}(\mathbb{R}^n)$ can be expressed

$$\begin{aligned} M = & M_{[n]}^{(1)} + M_{[n]}^{(2)} + M_{[n-1, 1]}^{(1)} + M_{[n-1, 1]}^{(2)} \\ & + M_{[n-1, 1]}^{(3)} + M_{[n-2, 2]}^{(1)} + M_{[n-2, 1, 1]}^{(1)}, \end{aligned} \quad (38)$$

where the blocks $M_{\lambda}^{(k)}$ are to be defined; this decomposition is fundamental for analyzing both the symmetry and invariants of S_n -equivariant linear maps.

B.1 Realization of S_3 irreps in $\text{End}(\mathbb{R}^3)$

Let

$$P_{ij} = u_i u_j \quad (39)$$

and

$$Q = 1 - P \quad (40)$$

be the orthogonal projections onto subspaces U and W , respectively. We can now write

$$\begin{aligned} M_{[3]}^{(1)} &= PMP, \\ M_{[2, 1]}^{(1)} &= PMQ, \\ M_{[2, 1]}^{(2)} &= QMP, \\ M_{QQ} &= QMQ; \end{aligned} \quad (41)$$

only M_{QQ} remains to be decomposed. Notice the sign representation

$$M_{[1, 1, 1]} = \frac{1}{2} Q (M - M^T) Q, \quad (42)$$

and, with

$$S = \frac{1}{2} Q (M + M^T) Q, \quad (43)$$

the remaining trivial copy

$$M_{[n]}^{(2)} = \frac{\text{tr } S}{\text{tr } Q} Q. \quad (44)$$

Hence,

$$M_{[n-1, 1]}^{(3)} = S - M_{[n]}^{(2)} \quad (45)$$

completes the isotypic decomposition of S .

That the projections onto distinct irreducible sectors are pairwise orthogonal facilitates a comprehensive and invariant overview of how each irreducible sector contributes to M .

These quantities admit the following interpretations: 1) $M_{[n]}^{(1)}$ captures the global mean of M , invariant under all row and column permutations, 2) $M_{[n]}^{(2)}$ reflects the isotropic residual in the symmetric fluctuations, 3) $M_{[n-1, 1]}^{(1)}$ quantifies the row-wise bias of the projected deviations, 4) $M_{[n-1, 1]}^{(2)}$ quantifies the column-wise bias of the projected deviations, 5) $M_{[n-1, 1]}^{(3)}$ captures the diagonal heterogeneity in residual overlaps, and 6) $M_{[n-2, 1, 1]}$ measures directional skew in the antisymmetric part.

C Compressible Euler

The compressible Euler equations in two-spatial dimensions can be expressed in terms of four continuity equations, each of which is of the form

$$\partial_t \rho_c + \nabla \cdot \mathbf{J}_c = 0, \quad (46)$$

where ρ_c is a conserved density, \mathbf{J}_c is the associated conserved current, and c designates mass, momentum, and energy. Equation 46 follows directly from symmetry arguments: invariance under time translation yields energy conservation, spatial translation invariances implies momentum conservation, and an underlying global phase symmetry provides mass conservation. When Equation 46 is defined with periodic boundary conditions, the volume integrals of the conserved densities remain exact invariants for all time. Thus, both the local continuity relations and their associated global constraints must be respected: the domain-integrated mass, the two Cartesian components of momentum, and the total energy may not drift at any time during the rollout. Any surrogate or reduced-order model that aspires to physical fidelity must therefore honour these integral invariants, in addition to satisfying the differential conservation laws Equation 46.

C.1 Integral Invariants

For definiteness, we show that mass, momentum, and energy are conserved in this system. To this end, recall that

$$J_{\text{mass}}^j = \rho_{\text{mass}} v^j \quad (47a)$$

$$J_{\text{mom}}^{ij} = \rho_{\text{mass}} v^i v^j + p \delta^{ij} \quad (47b)$$

$$J_{\text{energy}}^j = (\rho_{\text{energy}} + p) v^j \quad (47c)$$

where p is the pressure and δ_{ij} is the Kronecker delta. Having introduced pressure as a fifth dynamical variable, a constitutive relation is needed in order to arrive at a closed system of equations, which is achieved on writing the energy density as

$$\rho_{\text{energy}} = \rho_{\text{mass}} e + \frac{1}{2} \rho_{\text{mass}} |\mathbf{v}|^2, \quad (48)$$

where the specific internal energy e is related to the pressure, and using the ideal-gas law

$$p = (\gamma - 1) \rho_{\text{mass}} e, \quad (49)$$

with $\gamma = 1.4$ the adiabatic index of a diatomic gas.

While the continuity equations control the pointwise evolution of the densities, global conservation guarantees that the total amount of each conserved quantity is invariant under the flow map. Integrating the continuity equation for any density ρ_c over the periodic domain Ω and applying integration by parts (or, equivalently, the divergence theorem) yields

$$\frac{d}{dt} \int_{\Omega} \rho_c d\mathbf{A} + \underbrace{\int_{\partial\Omega} \mathbf{J}_c \cdot \mathbf{n} dS}_{\text{vanishes for periodic } \Omega} = 0. \quad (50)$$

Therefore,

$$Q_c(t) = \int_{\Omega} \rho_c d\mathbf{A} \quad (51)$$

is an integral of motion. This statement precludes secular drift of mass, momentum, or energy in long simulations, and serves as a primary evaluation metric for surrogate models. Note that the Navier-Stokes equations can also be expressed in the form Equation 46 and therefore also admit mass, momentum, and energy as conserved variables. However, in order to sensibly train a neural network on both Compressible Euler and Navier-Stokes, one should attach to the model input an indication of whether or not J_{mom} contains a viscous term.

D Supplementary Figures

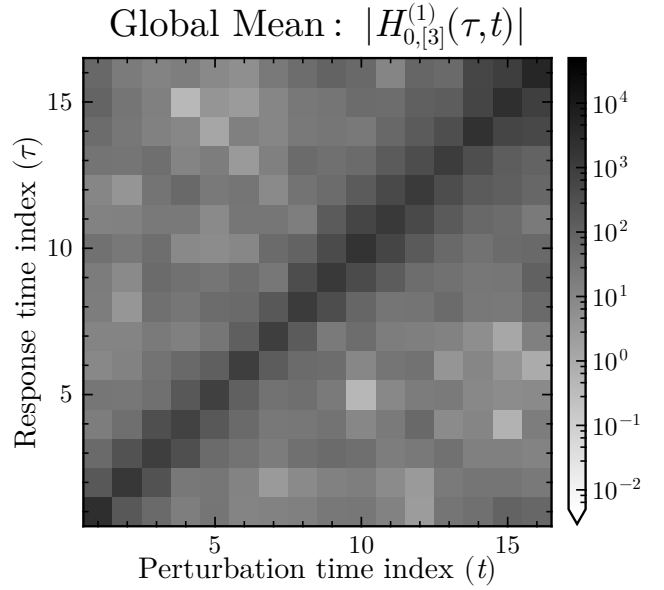


Figure 9: Sector norm of the response function between two loss gradients as a function of time separation (UNet).

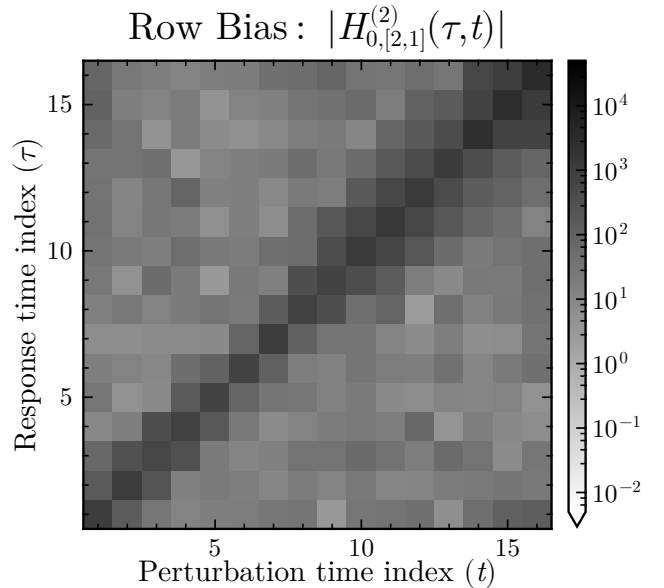


Figure 10: Sector norm of the response function between two loss gradients as a function of time separation (UNet).

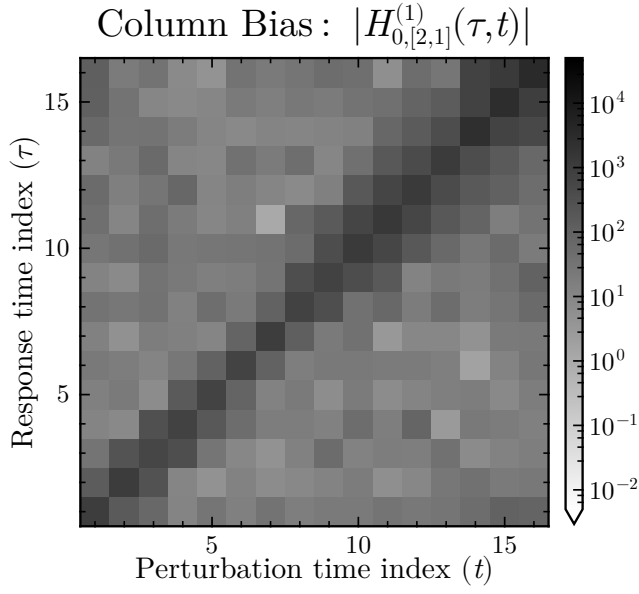


Figure 11: Sector norm of the response function between two loss gradients as a function of time separation (UNet).

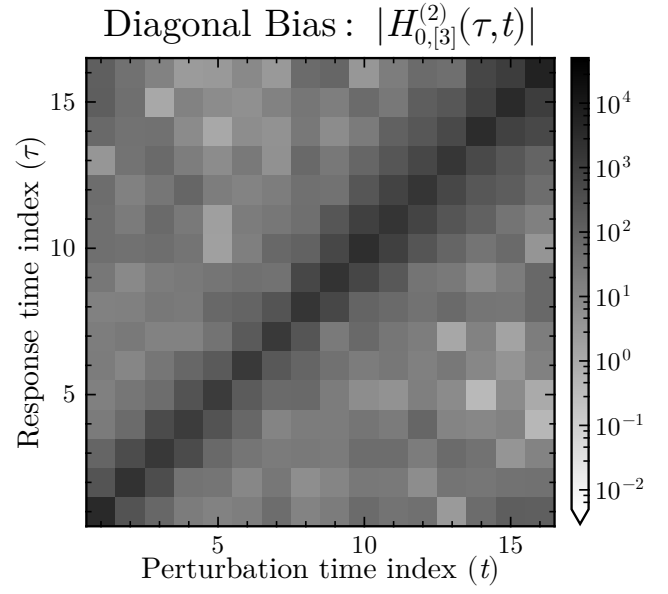


Figure 13: Sector norm of the response function between two loss gradients as a function of time separation (UNet).

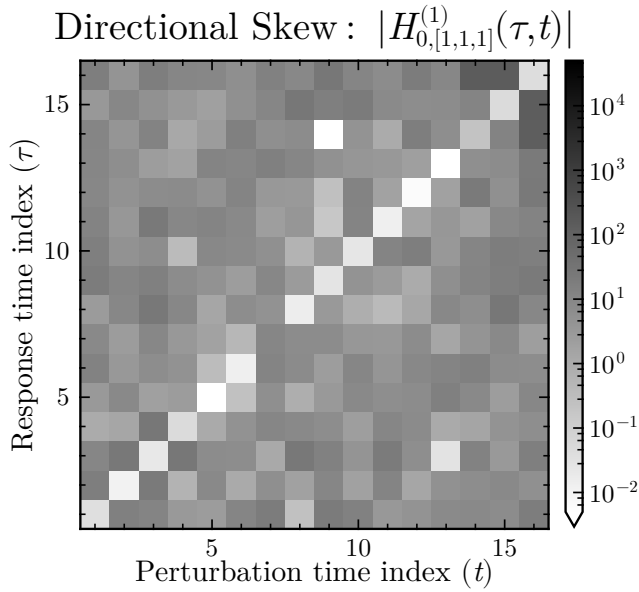


Figure 12: Sector norm of the response function between two loss gradients as a function of time separation (UNet).

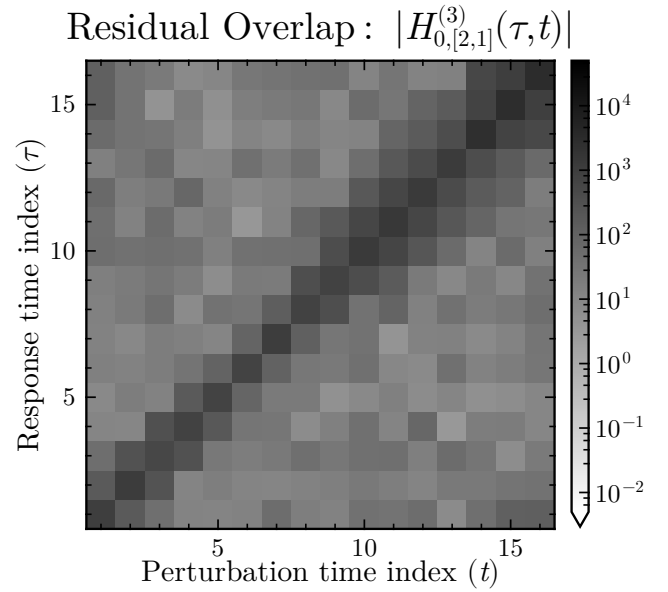


Figure 14: Sector norm of the response function between two loss gradients as a function of time separation (UNet).

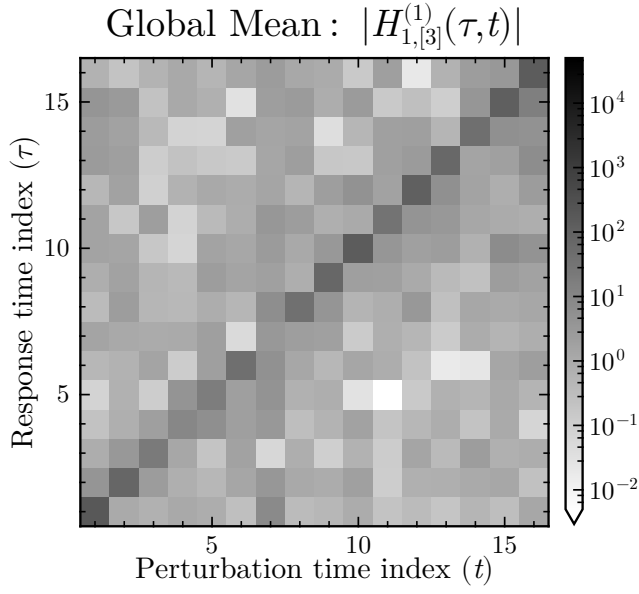


Figure 15: Sector norm of the response function between two loss gradients as a function of time separation (UNet).

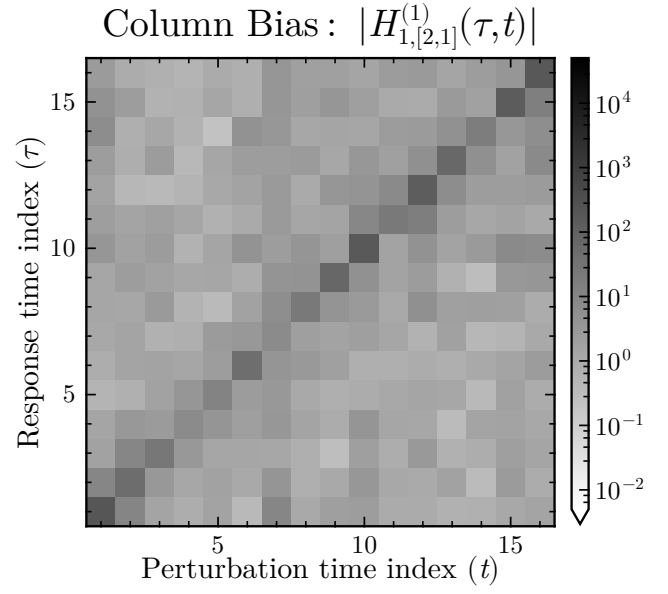


Figure 17: Sector norm of the response function between two loss gradients as a function of time separation (UNet).

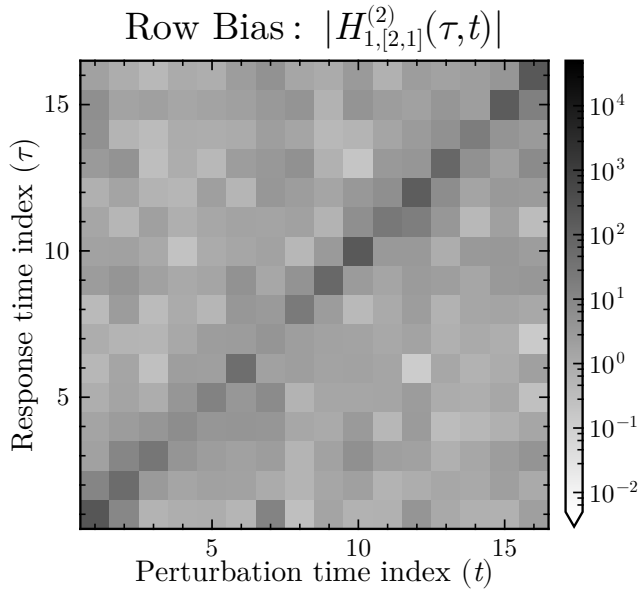


Figure 16: Sector norm of the response function between two loss gradients as a function of time separation (UNet).

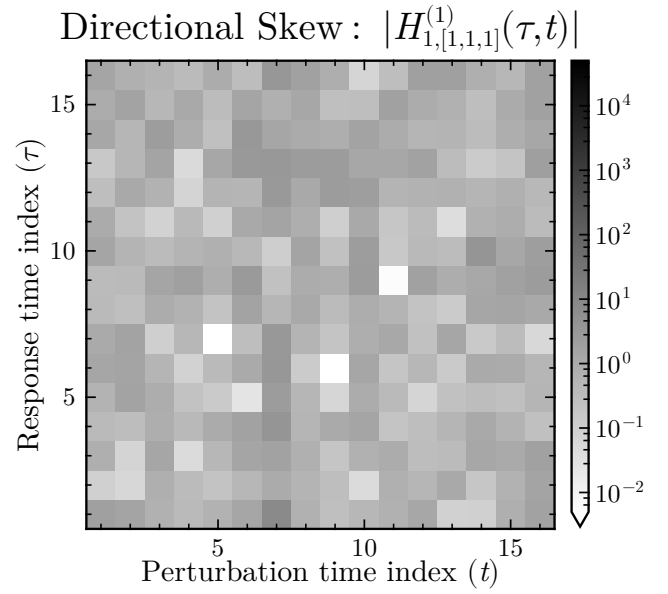


Figure 18: Sector norm of the response function between two loss gradients as a function of time separation (UNet).

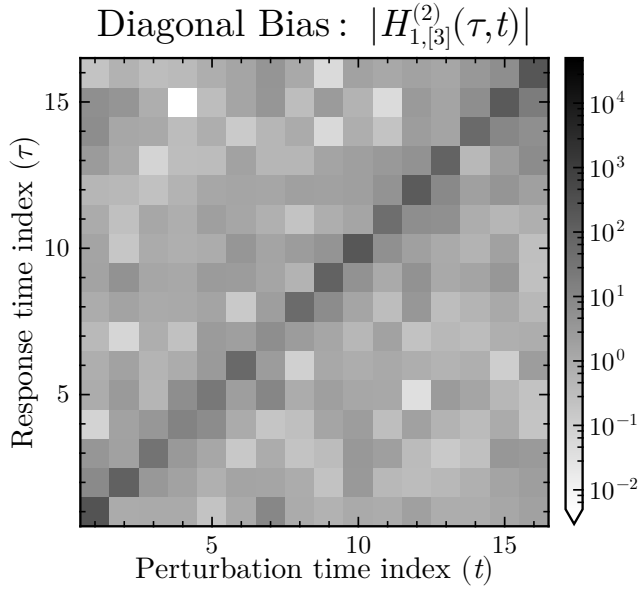


Figure 19: Sector norm of the response function between two loss gradients as a function of time separation (UNet).

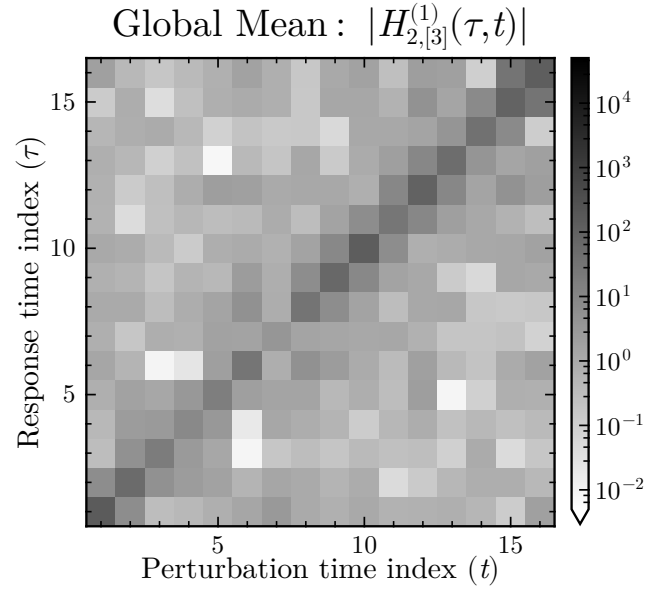


Figure 21: Sector norm of the response function between two loss gradients as a function of time separation (UNet).

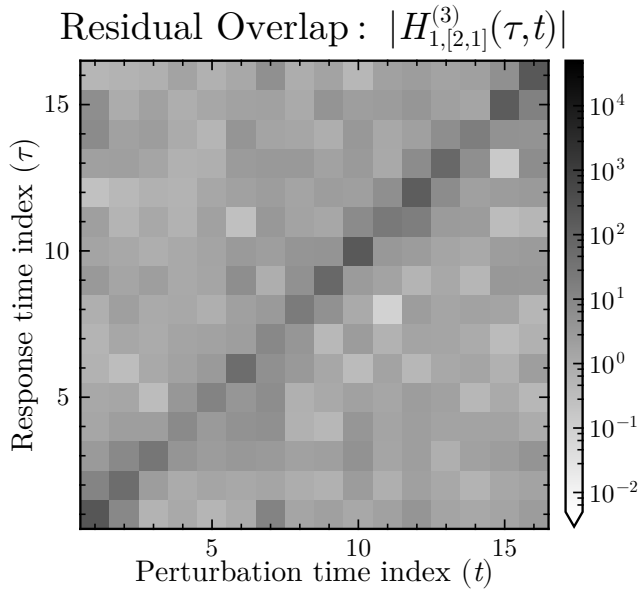


Figure 20: Sector norm of the response function between two loss gradients as a function of time separation (UNet).

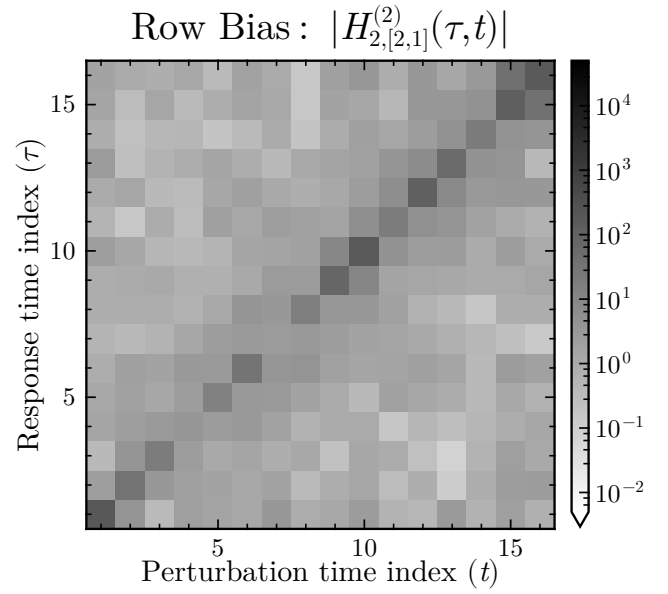


Figure 22: Sector norm of the response function between two loss gradients as a function of time separation (UNet).

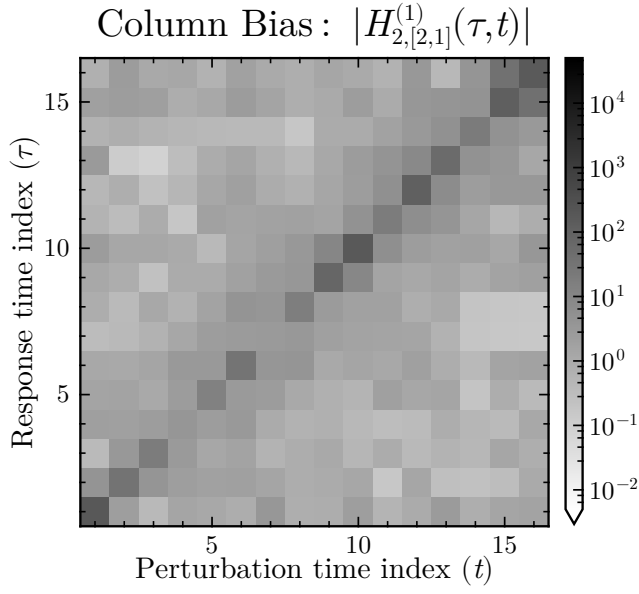


Figure 23: Sector norm of the response function between two loss gradients as a function of time separation (UNet).

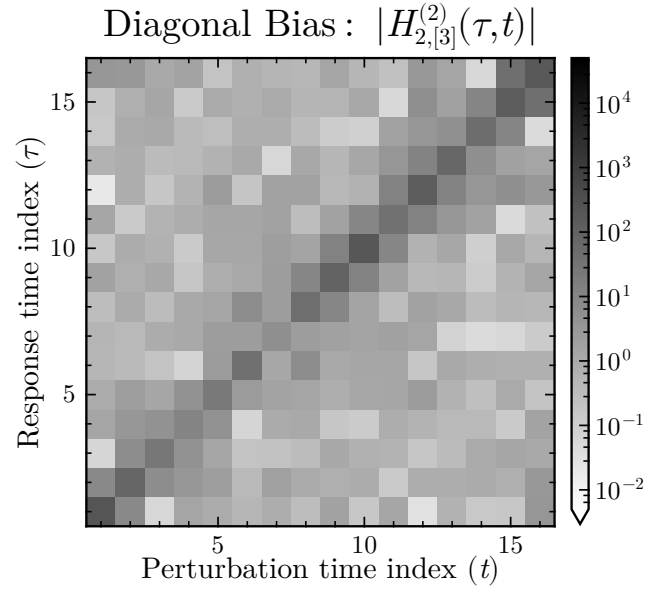


Figure 25: Sector norm of the response function between two loss gradients as a function of time separation (UNet).

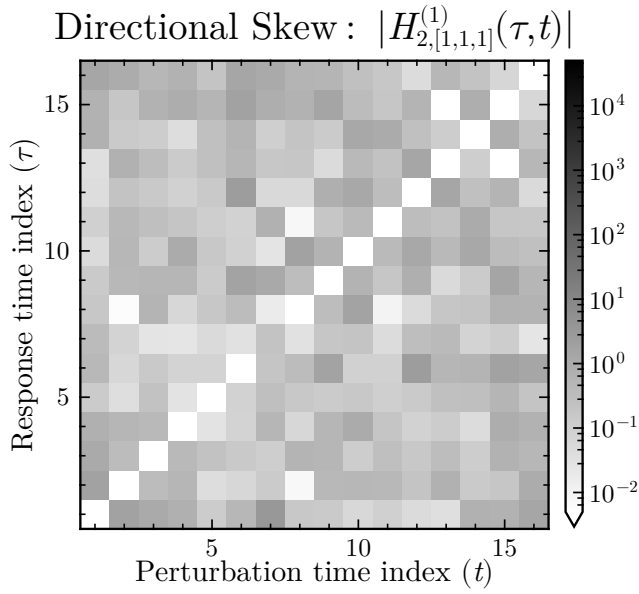


Figure 24: Sector norm of the response function between two loss gradients as a function of time separation (UNet).

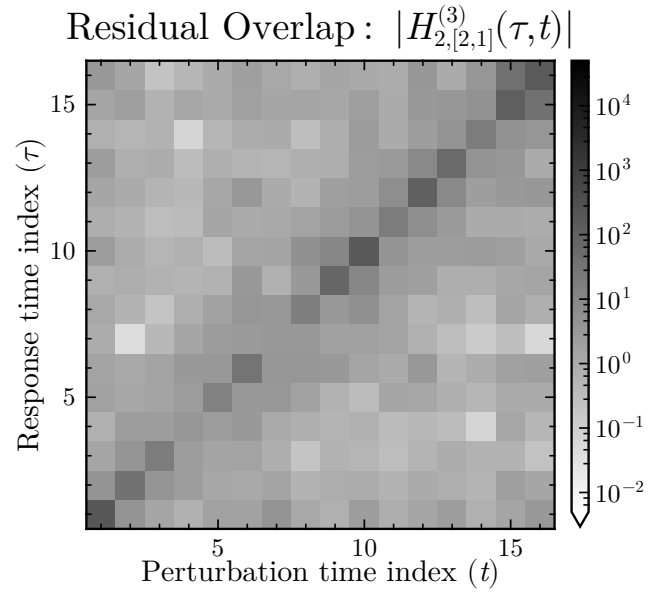


Figure 26: Sector norm of the response function between two loss gradients as a function of time separation (UNet).

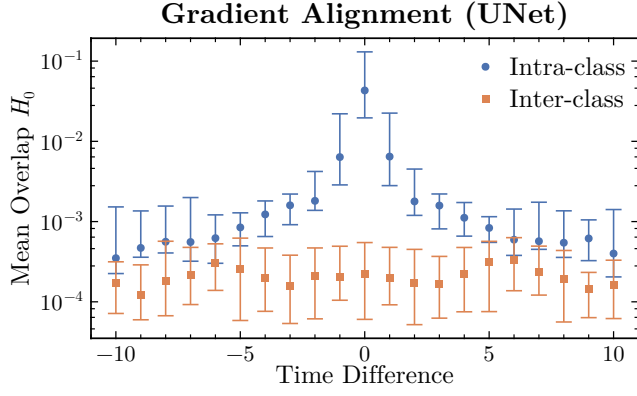


Figure 27: Average overlap of loss gradients as a function of time difference between their associated example inputs (UNet).

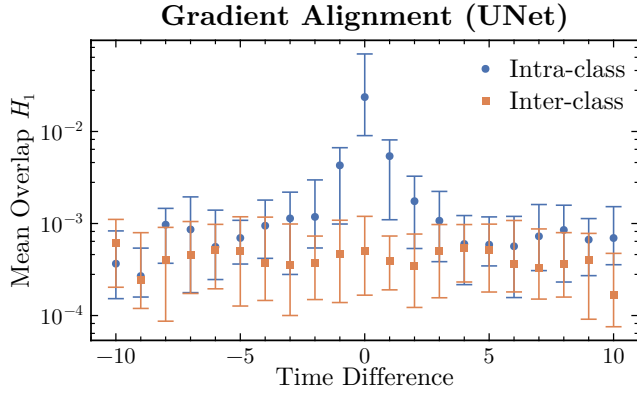


Figure 28: Average overlap of loss gradients as a function of time difference between their associated example inputs (UNet).

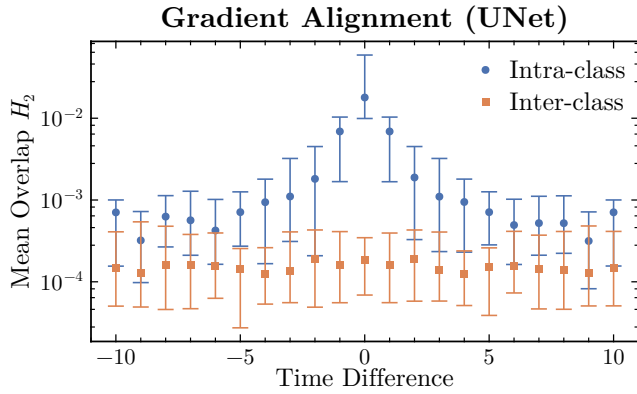


Figure 29: Average overlap of loss gradients as a function of time difference between their associated example inputs (UNet).

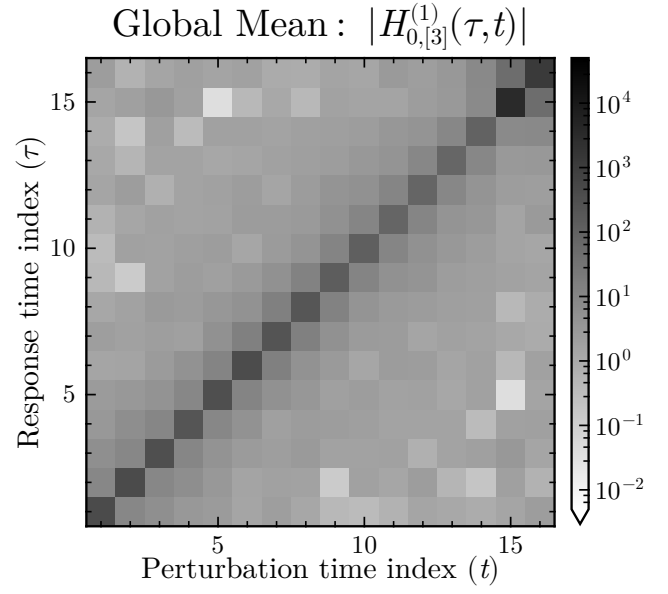


Figure 30: Sector norm of the response function between two loss gradients as a function of time separation (ViT).

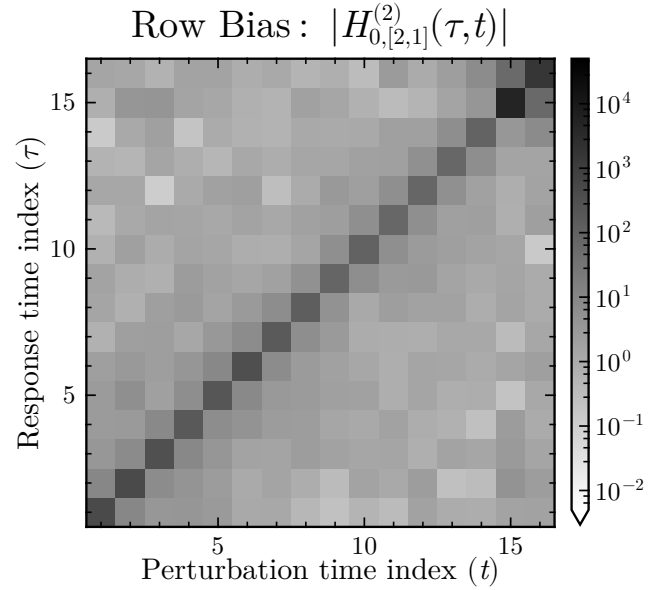


Figure 31: Sector norm of the response function between two loss gradients as a function of time separation (ViT).

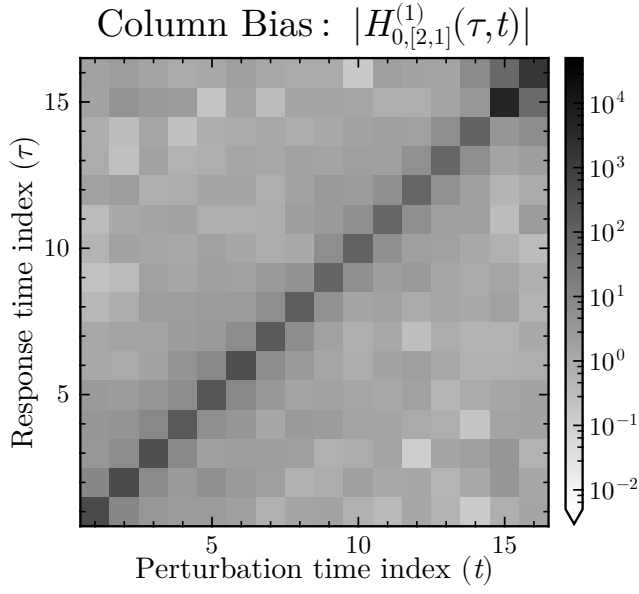


Figure 32: Sector norm of the response function between two loss gradients as a function of time separation (ViT).

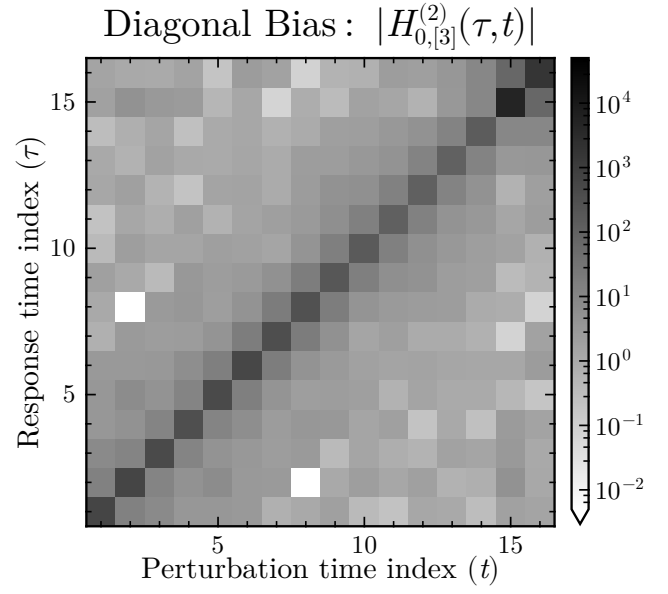


Figure 34: Sector norm of the response function between two loss gradients as a function of time separation (ViT).

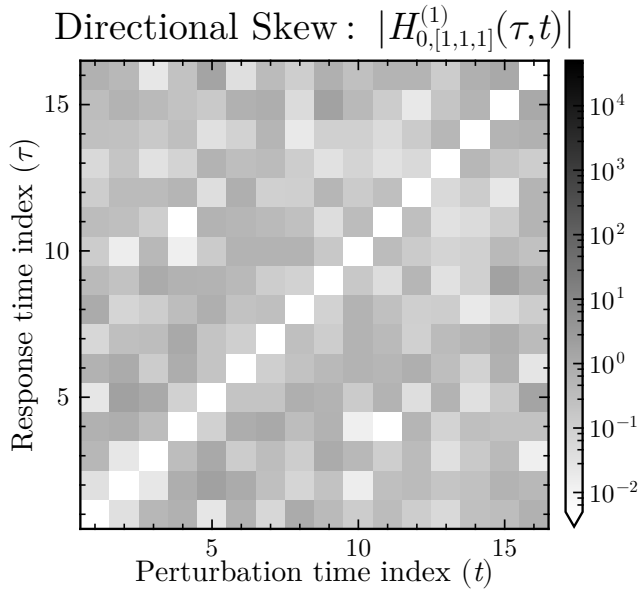


Figure 33: Sector norm of the response function between two loss gradients as a function of time separation (ViT).

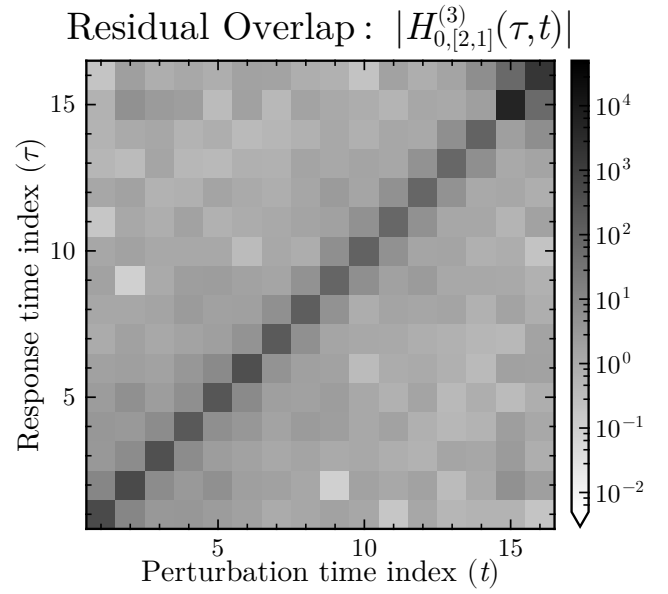


Figure 35: Sector norm of the response function between two loss gradients as a function of time separation (ViT).

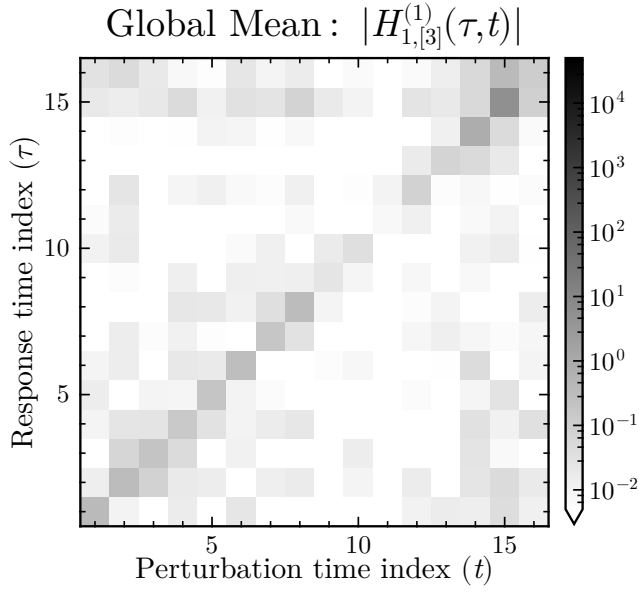


Figure 36: Sector norm of the response function between two loss gradients as a function of time separation (ViT).

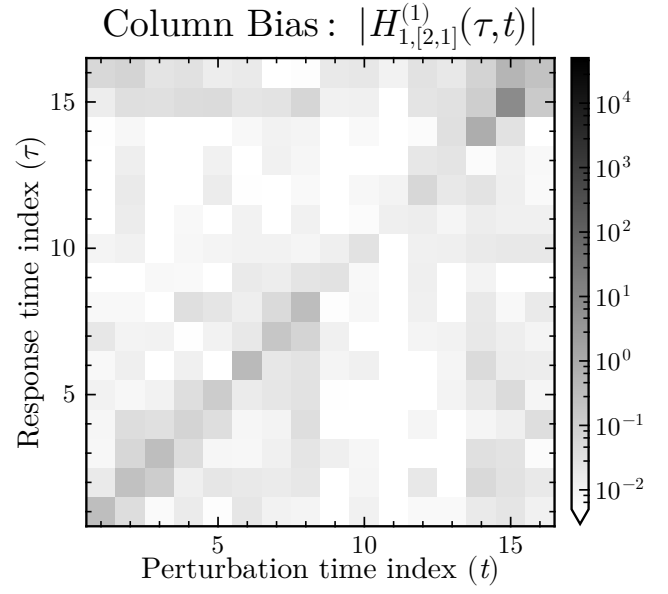


Figure 38: Sector norm of the response function between two loss gradients as a function of time separation (ViT).

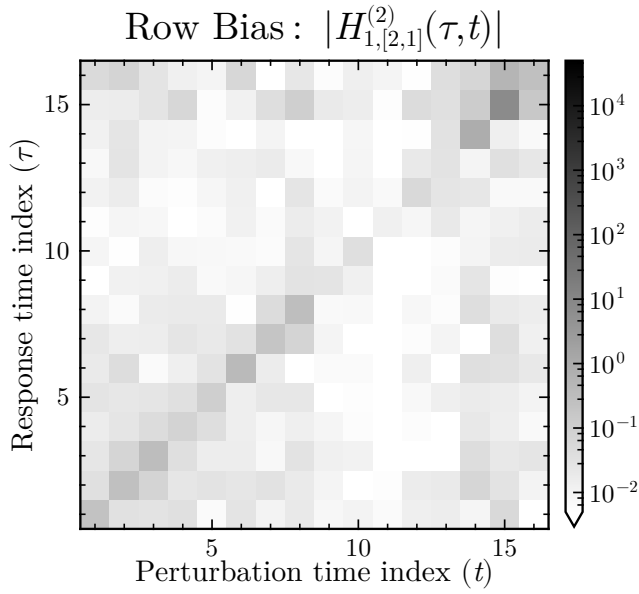


Figure 37: Sector norm of the response function between two loss gradients as a function of time separation (ViT).

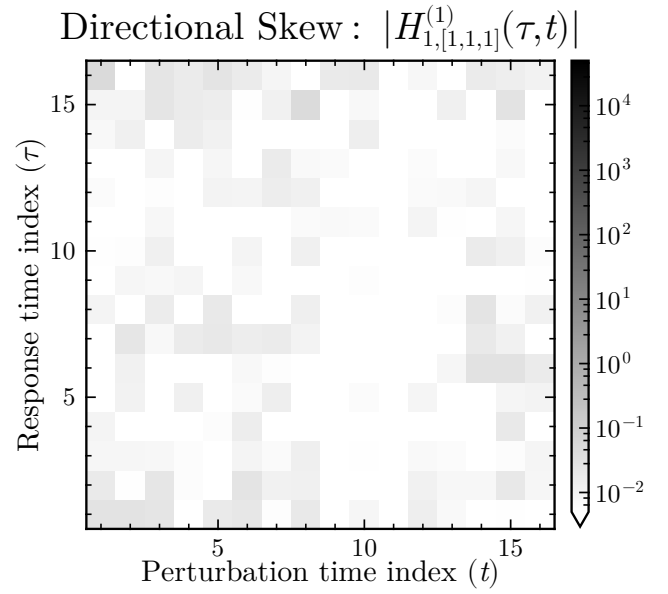


Figure 39: Sector norm of the response function between two loss gradients as a function of time separation (ViT).

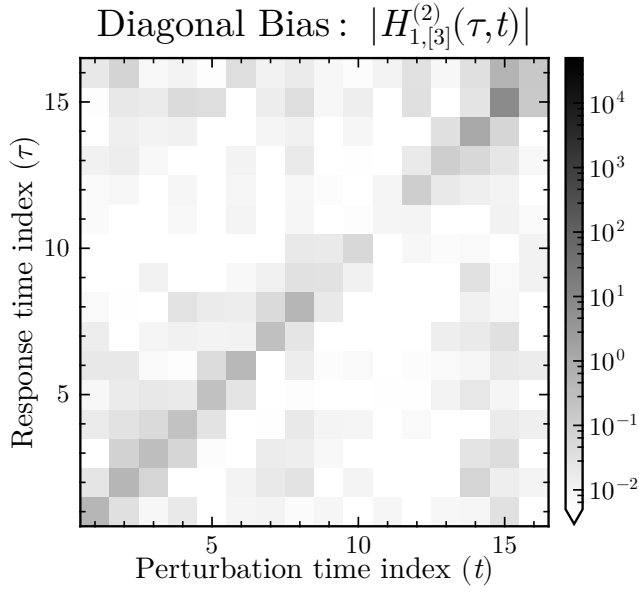


Figure 40: Sector norm of the response function between two loss gradients as a function of time separation (ViT).

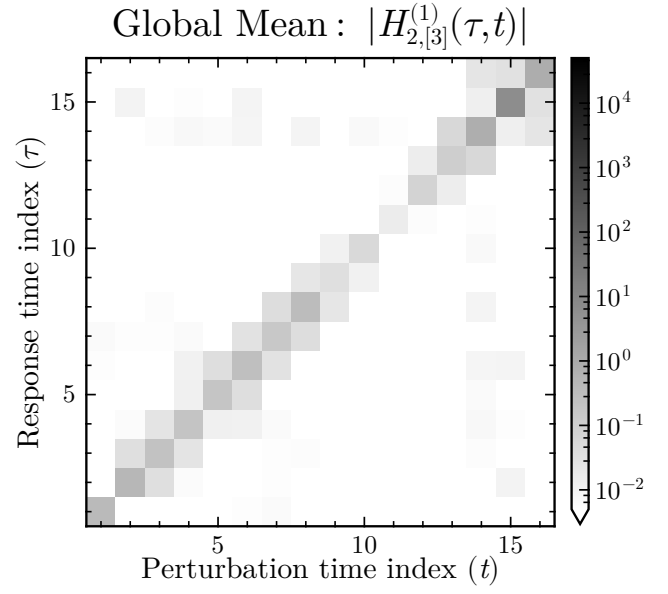


Figure 42: Sector norm of the response function between two loss gradients as a function of time separation (ViT).

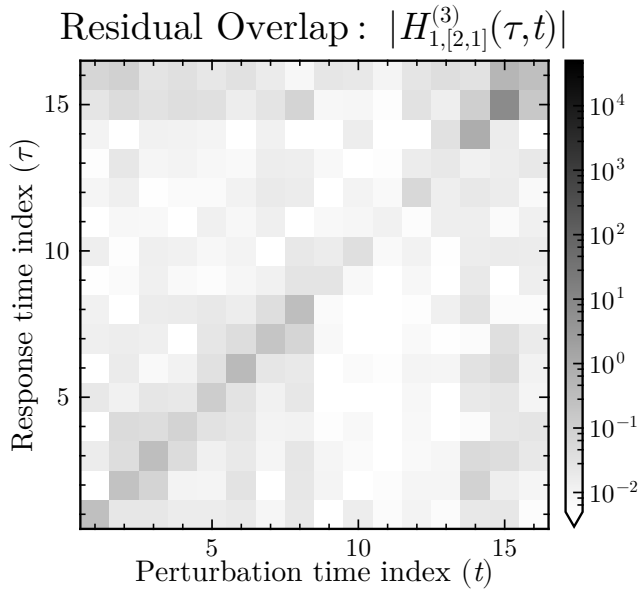


Figure 41: Sector norm of the response function between two loss gradients as a function of time separation (ViT).

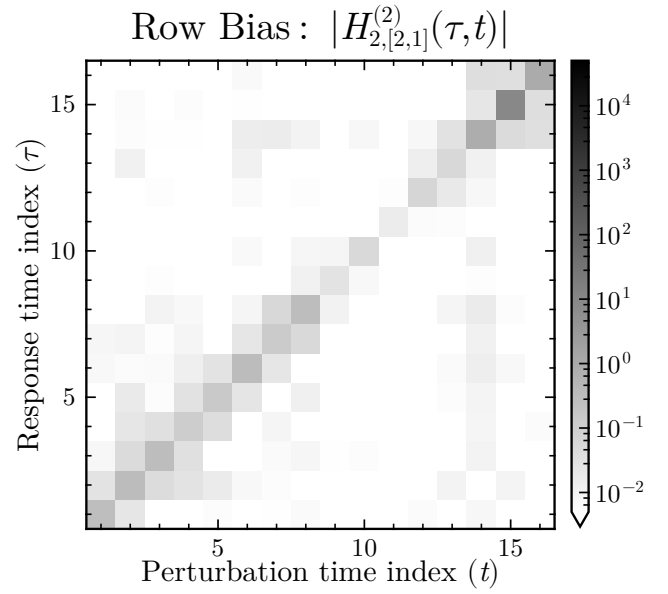


Figure 43: Sector norm of the response function between two loss gradients as a function of time separation (ViT).

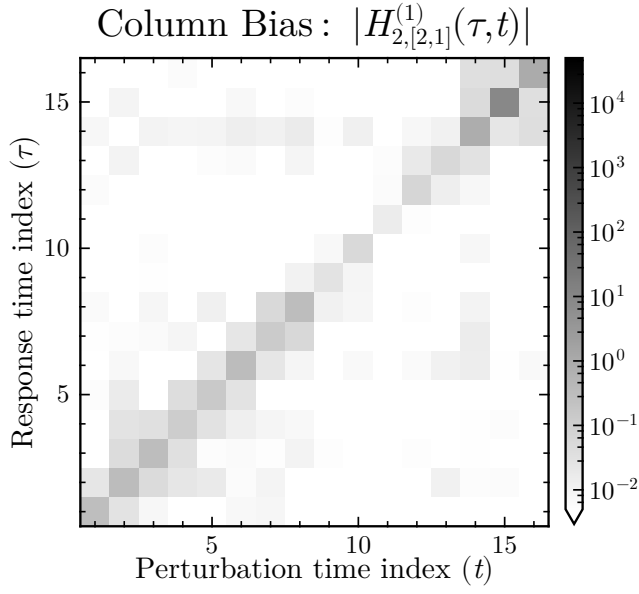


Figure 44: Sector norm of the response function between two loss gradients as a function of time separation (ViT).

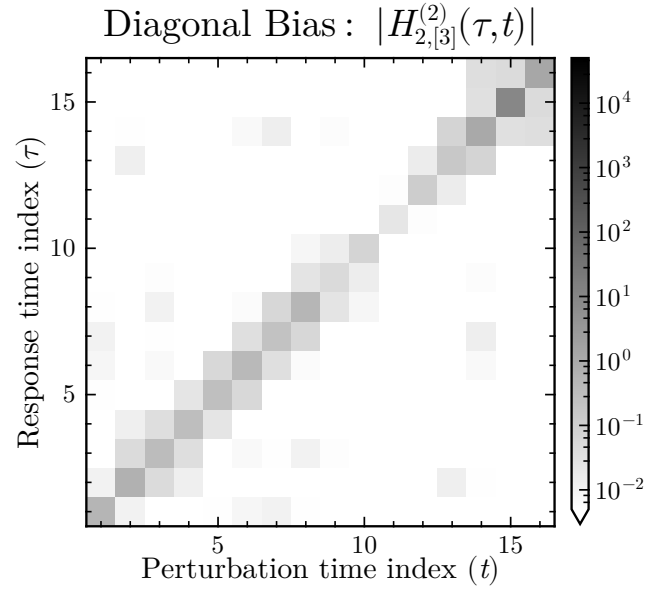


Figure 46: Sector norm of the response function between two loss gradients as a function of time separation (ViT).

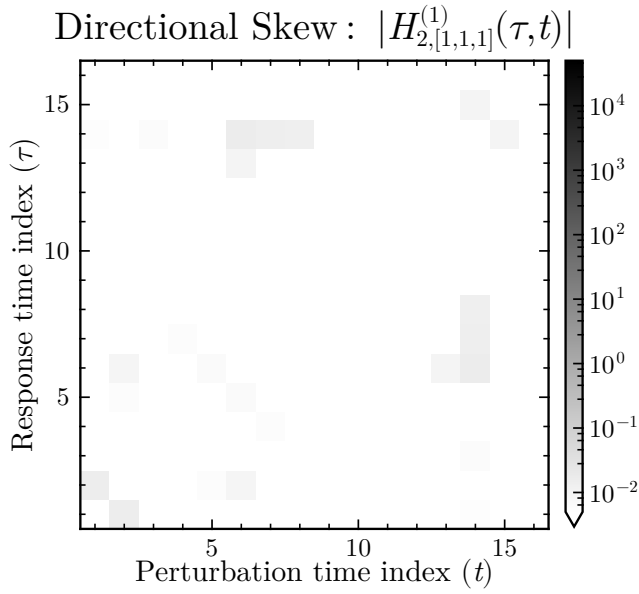


Figure 45: Sector norm of the response function between two loss gradients as a function of time separation (ViT).

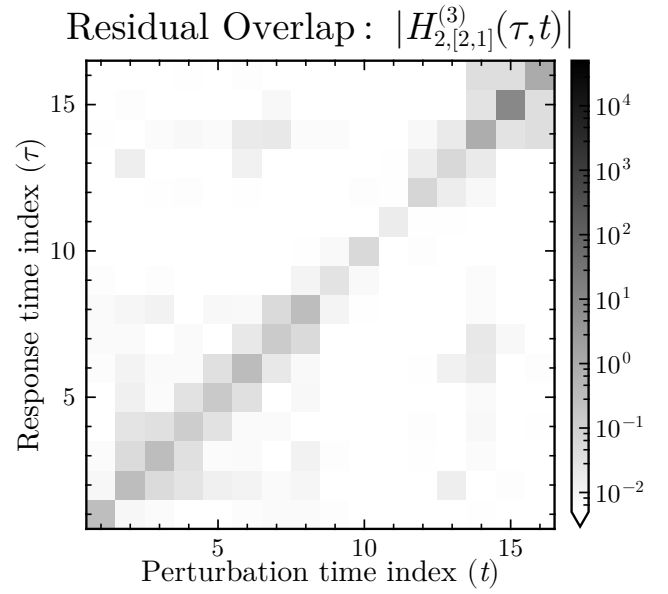


Figure 47: Sector norm of the response function between two loss gradients as a function of time separation (ViT).

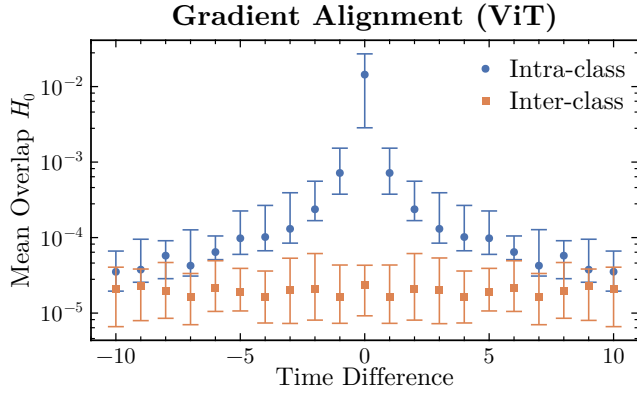


Figure 48: Average overlap of loss gradients as a function of time difference between their associated example inputs (ViT).

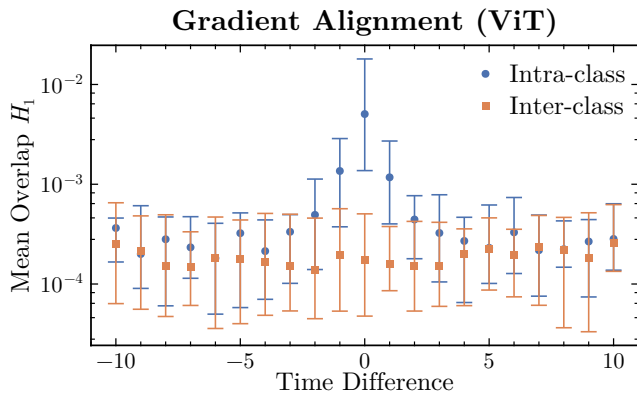


Figure 49: Average overlap of loss gradients as a function of time difference between their associated example inputs (ViT).

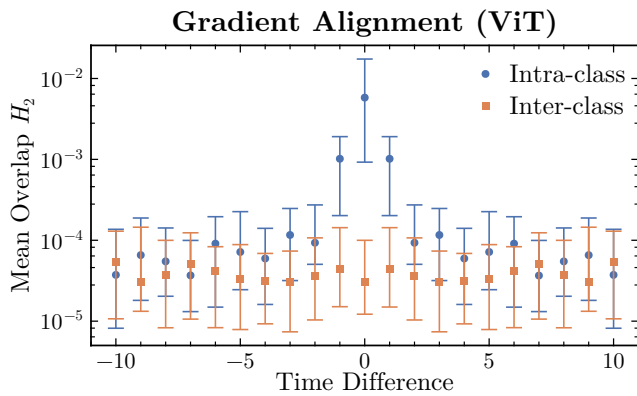


Figure 50: Average overlap of loss gradients as a function of time difference between their associated example inputs (ViT).